nature biomedical engineering

ARTICLES

https://doi.org/10.1038/s41551-021-00757-2

Check for updates

Single-cell-resolved differentiation of human induced pluripotent stem cells into pancreatic duct-like organoids on a microwell chip

Sandra Wiedenmann[1,9], Markus Breunig[2,9], Jessica Merkle[2], Christine von Toerne[3], Tihomir Georgiev[1], Michel Moussus[1], Lucas Schulte[2], Thomas Seufferlein[2], Michael Sterr[4,5], Heiko Lickert[4,5,6,7], Stephanie Ellen Weissinger[8], Peter Möller[8], Stefanie M. Hauck[3], Meike Hohwieler[2]✉, Alexander Kleger[2]✉ and Matthias Meier[1,7]✉

Creating in vitro models of diseases of the pancreatic ductal compartment requires a comprehensive understanding of the developmental trajectories of pancreas-specific cell types. Here we report the single-cell characterization of the differentiation of pancreatic duct-like organoids (PDLOs) from human induced pluripotent stem cells (hiPSCs) on a microwell chip that facilitates the uniform aggregation and chemical induction of hiPSC-derived pancreatic progenitors. Using time-resolved single-cell transcriptional profiling and immunofluorescence imaging of the forming PDLOs, we identified differentiation routes from pancreatic progenitors through ductal intermediates to two types of mature duct-like cells and a few non-ductal cell types. PDLO subpopulations expressed either mucins or the cystic fibrosis transmembrane conductance regulator, and resembled human adult duct cells. We also used the chip to uncover ductal markers relevant to pancreatic carcinogenesis, and to establish PDLO co-cultures with stellate cells, which allowed for the study of epithelial–mesenchymal signalling. The PDLO microsystem could be used to establish patient-specific pancreatic duct models.

Pancreatic ductal cells are organized in tubular ductal networks. Ductal cells secrete a bicarbonate-rich alkaline aqueous solution to transport zymogens produced by acinar cells[1]. Dysfunction of ductal cells can affect fluid composition in cystic fibrosis, leading to a subsequent deterioration of the entire organ[1,2]. Dysplastic events within the ductal epithelium can lead to pancreatic ductal adenocarcinoma (PDAC)[3–5], one of the most lethal cancer types[6]. Shortage of healthy and early disease-affected primary ductal material hampers the discovery of biomarkers for diagnostics and drug development. To overcome the limitation imposed by this shortage of donor material, lumen-forming pancreatic organoid cultures have been derived from resected healthy and diseased pancreata[7,8]. Pancreatic organoids preserve the cellular heterogeneity of the human pancreas and can be used to establish functional tests or discover biomarkers for PDAC in vitro[9,10]. Pancreatic cancer-derived organoids: (1) exhibit an undefined genetic background, (2) are generated from a tumour origin, (3) mimic the end stage of cancer, and (4) are unsuitable for biomarker discovery in the earliest stages of pancreatic dysplasia[11]. Adult human pancreatic organoids[12,13] are challenging to establish and to culture in an untransformed state and, moreover, do not provide access to developmental intermediates. Lineage-committed pancreatic ductal cells generated from human pluripotent stem cells (hPSCs) could be an alternative source of pancreatic organoids to overcome these obstacles[14,15].

The engineering and translation of in vitro ductal disease models require a full mechanistic understanding of the in vitro ductal differentiation landscape, cell-type composition, and functionality at the ductal stage. Unfortunately, there is a dearth of knowledge on human embryonic duct development. Previous studies in rodents revealed that all pancreatic cell lineages evolve from pancreatic-progenitor cells, a common pancreatic cell type derived from endoderm[16]. Pancreatic progenitors organized in the pancreatic bud undergo tip–trunk patterning. The acinar cells evolve from the tip domain, and ductal cells together with subsequently delaminating endocrine cell types evolve from presumably bipotent trunk cells[17,18]. Time-resolved immunostaining of developing human embryos suggest a similar mechanism for human pancreatic cell-type development[19]. Recently, we and others developed a differentiation protocol to guide hPSCs to form pancreatic duct-like organoids (PDLOs)[20,21]. Single-cell RNA sequencing (scRNA-seq) has become the method of choice for studying cell differentiation in organoids or tissue development to reveal cell heterogeneity, quantify cell types, and resolve molecular mechanisms leading to cell lineage bifurcations and their subsequent transitions[22]. scRNA-seq of primary human pancreatic tissue is well-established[23–28], but to our knowledge, there is no time-resolved single-cell transcriptional roadmap of developmental trajectories from hPSCs towards ducts.

Organoid formation and stem cell differentiation are non-linear deterministic systems; thus, slight variations in initial conditions

[1]Helmholtz Pioneer Campus, Helmholtz Zentrum München, Neuherberg, Germany. [2]Department of Internal Medicine I, Ulm University Hospital, Ulm, Germany. [3]Research Unit Protein Science, Helmholtz Zentrum München, Munich, Germany. [4]Institute of Diabetes and Regeneration Research, Helmholtz Zentrum München, Neuherberg, Germany. [5]German Center for Diabetes Research (DZD), Neuherberg, Germany. [6]Institute of Stem Cell Research, Helmholtz Zentrum München, Neuherberg, Germany. [7]School of Medicine, Technical University of Munich, Munich, Germany. [8]Institute for Pathology, Ulm University Hospital, Ulm, Germany. [9]These authors contributed equally: Sandra Wiedenmann, Markus Breunig. ✉e-mail: meike.hohwieler@uni-ulm.de; alexander.kleger@uni-ulm.de; matthias.meier@helmholtz-muenchen.de

can influence the outcome of the process. Therefore, controlling the initial organoid size and shape in microwells is thought to improve the reproducibility of differentiation[29,30]. Microwells are the most simplistic chip technologies for assisting the formation of organoids and their culture. Further, microenvironmental signals of confined organoids and the organoids themselves are directly accessible for downstream analysis from the open microwells. Thus, a microwell chip design offers simple cell sample collection for scRNA-seq, and proteome and/or secretome analyses during ductal differentiation of hPSCs.

In this study, we designed a microwell chip to generate defined 3D aggregates of human induced pluripotent stem cell (hiPSC)-derived pancreatic progenitors and, subsequently, to induce their differentiation towards PDLOs. Time-resolved scRNA-seq combined with cleared immunofluorescence imaging provided a deep understanding of in vitro ductal cell-type differentiation. By defining the emergent cell types at each stage of differentiation on the basis of their gene-expression profiles and organoid structures, we provide a precise cell-by-cell description of the in vitro differentiation trajectory. Transcriptional data of PDLOs were complemented by their proteome and secretome, enabling the identification and validation of prognostic cancer markers. Thus, we show the applicability of hiPSC-derived PDLOs on a microwell chip for future ductal disease modelling.

Results

A microwell chip to form 3D aggregates from hiPSC-derived pancreatic progenitors. To enable engineering and long-term culture of duct-like organoids from hiPSC-derived pancreatic progenitors, we designed a microwell chip technology (Fig. 1a–d). The microwell chip was produced by soft lithography with polydimethylsiloxane (PDMS), where the casting moulds were prepared using 3D stereolithography printing (Supplementary Fig. 1a). Each microwell chip contained four hexagonal arrays with cone-shaped wells, and 12 round pillars surrounded each array. The function of the pillars was to retain an aqueous drop (20–40 µl) above the array by surface tension (Fig. 1a,b). A 180-µm-thin PDMS bottom layer allowed high-resolution imaging of confined organoids (Fig. 1c). Together with roundings between wells, the pillars enabled an efficient and homogeneous cell seeding process without blind spots. Details of the production method and workflow for cell seeding and culturing are given in Supplementary Fig. 1b. First, we validated the stem cell viability within differently sized microwells (150, 300 and 600 µm). Next, we systematically altered the initial cell number and well size to optimize the formation of hiPSC-derived aggregates of pancreatic progenitors. Pancreatic-progenitor aggregates formed on the microwell chip within 4 h with uniform size according to variable well diameters and cell numbers (Fig. 1d,e). A small number of cells (less than 50 cells per well) compromised the aggregation step in the microwells, and the generation of cell aggregates with diameters of more than about 250 µm is known to impair nutrient supply[31]. For the subsequent ductal differentiation, we selected an average initial pancreatic-progenitor-aggregate size of 96 µm (600 cells in 300-µm-diameter wells).

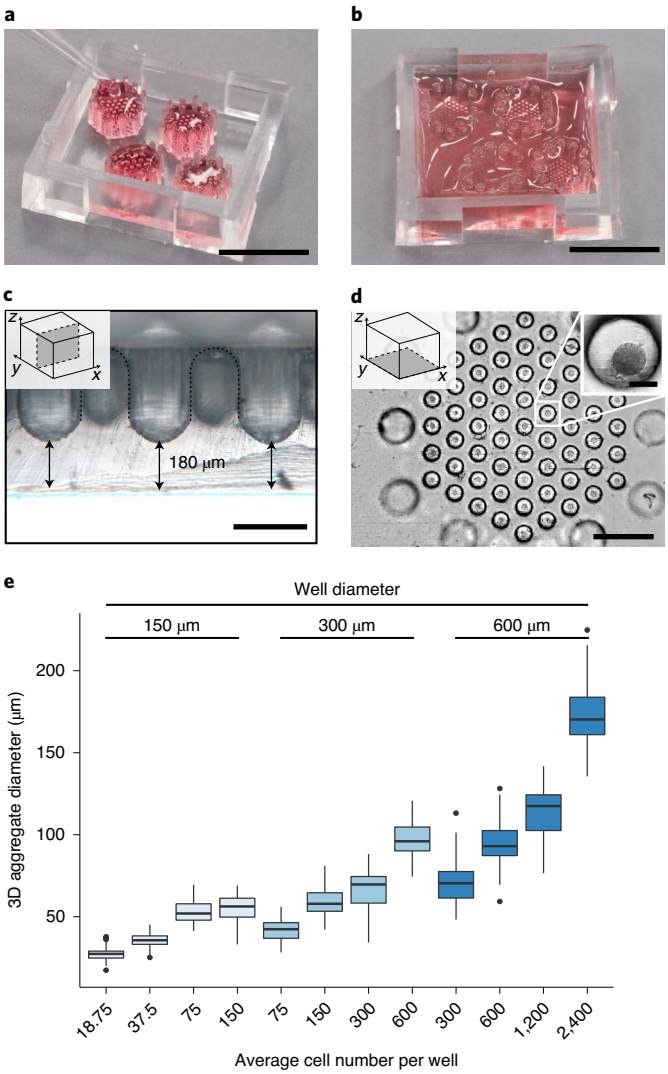

Fig. 1 | Microwell chips for generating and culturing 3D cell aggregates. **a**, Image of the microwell chip with four microwell arrays (top-down view). Each hexagonal array is surrounded by 12 pillars to keep fluid volume above the microwell. Cells were seeded in 20–40 µl medium. Scale bar, 1 cm. **b**, After cell seeding, the entire microwell chip was filled up to 800 µl media for long-term cell culture. Scale bar, 1 cm. **c**, Cross-sectional view of the microwell chip bottom. Scale bar, 300 µm. **d**, Bottom view of one microwell array. Scale bar, 1 mm. Inset: higher magnification of a pancreatic-progenitor-derived 3D aggregate formed from 600 cells. Scale bar, 100 µm. **e**, Aggregate size is dependent on the cell number and well diameter after 24 h of seeding pancreatic progenitors, including at least 58 pancreatic-progenitor-derived 3D aggregates from 3 different microwell arrays. Boxes show the median with the first and third quartiles, whiskers denote the 1.5× the interquartile range and outliers are shown as dots.

Ductal differentiation on the microwell chip. We differentiated 3D pancreatic-progenitor aggregates towards PDLOs using the microwell chip. Pancreatic progenitors generated in monolayer culture formed aggregates on the chip, followed by a two-step differentiation process with specific growth factors (Fig. 2a). Subsequently, pancreatic-progenitor aggregates underwent large morphological changes within the microwells, as indicated in the representative bright-field images (Fig. 2b and Supplementary Fig. 3a). In the first ductal induction phase, the uniform round-shaped pancreatic-progenitor aggregate structure was broken up by newly formed multi-layered epithelial protrusions (Fig. 2b). In the second ductal differentiation phase, multi-layered epithelium organoids reduced their number of layers and cystic organoids were segregated from the outer layer of the PDLOs. Notably, a few cystic PDLO structures remained connected to the multi-layered epithelial PDLOs at day 31 of differentiation. The morphological transformation of the PDLOs is visualized in Supplementary Video 1. High-resolution immunofluorescence images of cleared organoids confirmed cellular re-organization towards the end of phase 1 of ductal differentiation (Fig. 2c,d). Epithelial nature and pancreatic ductal identity of the cells at the final stage were confirmed by

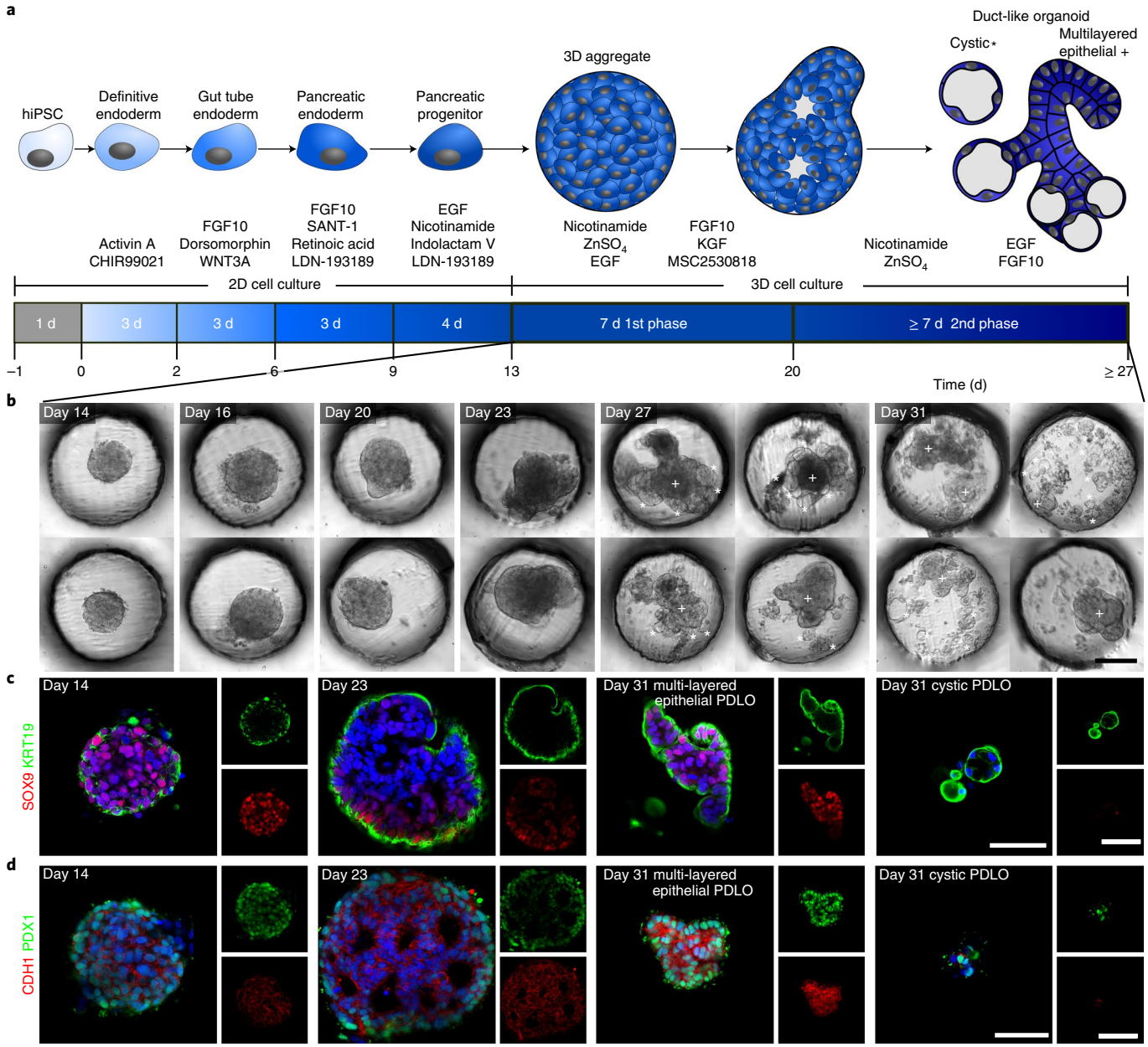

Fig. 2 | PDLO differentiation in the microwell chip. a, Schematic of cell differentiation from hiPSCs to PDLOs, showing supplements added to the culture medium and timeline for each stage. **b**, Representative bright-field images of 3D pancreatic-progenitor aggregates after 14, 16, 20, 23, 27 and 31 d of differentiation (DOD). Morphological changes of organoids during the first differentiation phase between 14 to 20 DOD, and formation of two morphologically distinct PDLO types within the second differentiation phase. Multi-layered epithelial PDLOs are marked with a cross and cystic types are marked with a star. See Supplementary Fig. 3a for overview images. **c**,**d**, Fluorescence images of the 3D aggregates along the time course of differentiation with co-stained ductal protein markers SOX9 and KRT19 (**c**) and PDX1 and CDH1 (**d**). A comprehensive set of progenitor and ductal markers is depicted in Supplementary Fig. 3b–e. The nucleus was counterstained with DAPI. Scale bars, 50 μm.

the upregulation of E-cadherin (CDH1), cytokeratin 19 (KRT19), aquaporin 5 (AQP5), mucin 1 (MUC1), carbonic anhydrase II (CA2), cytokeratin 7 (KRT7), claudin 1 (CLDN1) and cystic fibrosis transmembrane conductance regulator (CFTR) (Fig. 2c,d and Supplementary Fig. 3b). Expression of ductal markers, which were already detected at the pancreatic-progenitor stage, such as cytokeratin 8 (KRT8), SRY-box transcription factor 9 (SOX9), hepatocyte nuclear factor 1 homeobox B (HNF1B), and pancreatic and duodenal homeobox 1 (PDX1) were maintained in PDLOs (Fig. 2c,d and Supplementary Fig. 3b,c). By contrast, the progenitor marker homeobox protein NKX6-1, which becomes restricted to endocrine cells during pancreatic development, was downregulated at the protein level (Supplementary Fig. 3c). Stemness marker SRY-box 2 (SOX2) and octamer-binding transcription factor 4 (OCT4) were absent (Supplementary Fig. 3d), as were non-ductal pancreas markers, except in a few endocrine cells located at the periphery of PDLOs (Supplementary Fig. 3e). In agreement with the marker panel, a forskolin-induced swelling assay confirmed pancreatic ductal functionality (Supplementary Fig. 4). To demonstrate that the microwell chip-derived PDLOs are lineage-committed, we transplanted PDLOs differentiated until day 27 orthotopically into the pancreas of immunocompromised mice (Fig. 3a). PDLO

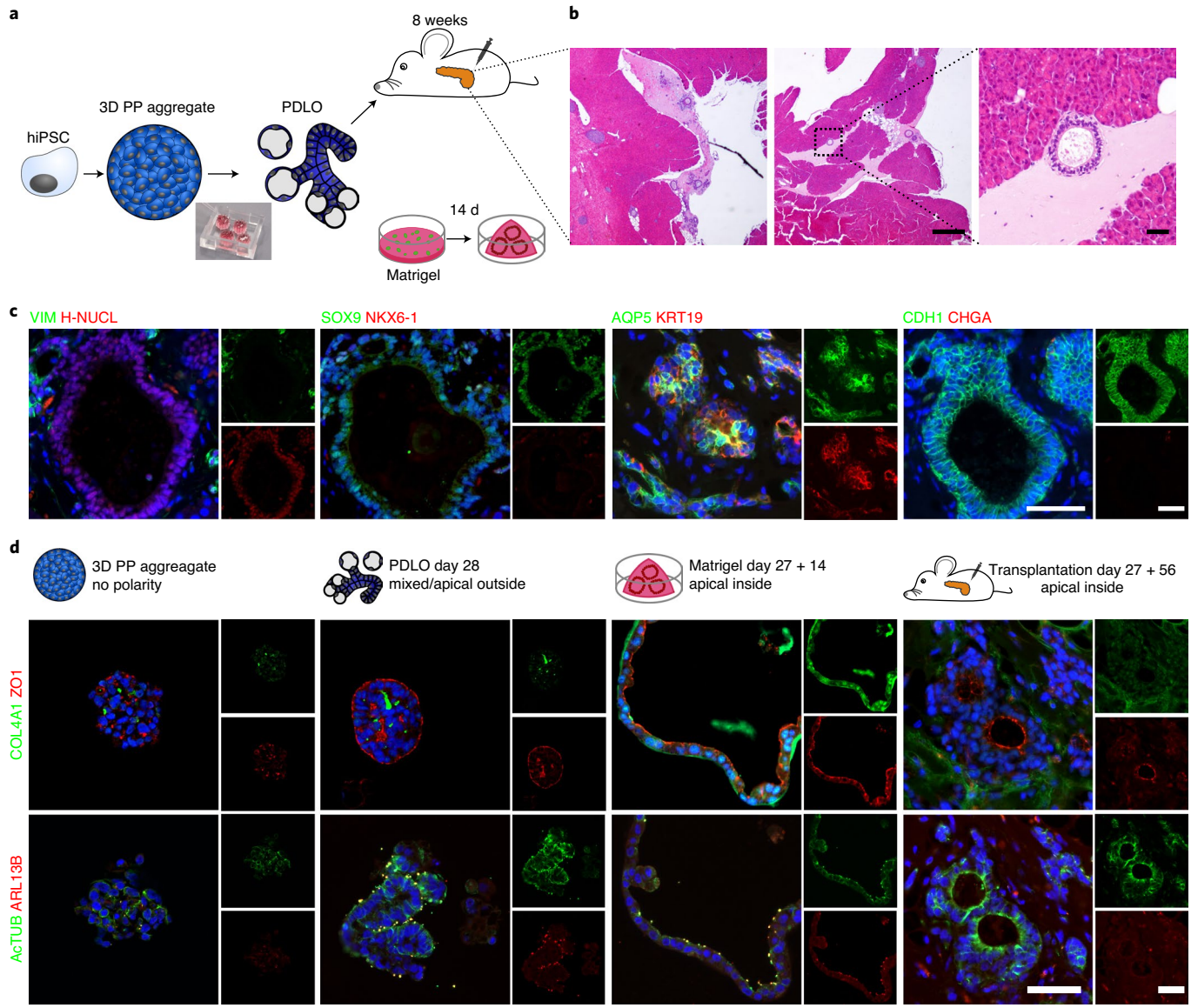

Fig. 3 | Apical-out polarity of the microwell chip-derived PDLOs switched upon orthotopic transplantation or embedding into Matrigel. a, Schematic of the Matrigel and orthotopic transplantation experiment. PDLOs were transplanted on day 27 and mice were euthanized after 8 weeks. PP, pancreatic progenitor. **b**, Haematoxylin and eosin staining and magnification of the engraftment site depicted by the dashed square ($n = 2$ mice). Scale bars, 500 µm (left and middle) and 50 µm (right). **c**, PDLOs formed human epithelial duct-like tissue in vivo. CHGA, chromogranin A; H-NUCL, human-specific nucleoli; VIM, vimentin. Scale bar, 50 µm. **d**, Immunofluorescence images of the apical markers ZO1 and acTUB and basal markers COL4A1 and ARL13B on 3D pancreatic-progenitor aggregates, PDLOs, Matrigel PDLOs and transplanted PDLOs. Complementary images are shown in Supplementary Fig. 5. Nuclei were counterstained with DAPI. Scale bars, 50 µm.

engraftments formed tubular duct-like tissue after eight weeks, homogeneously expressed epithelial ductal markers such as SOX9, KRT19, AQP5 and CDH1, and were negative for endocrine cell types (Fig. 3b,c).

PDLOs exhibited a predominant apical-out polarity, although apical markers tight junction protein-1 (ZO1), cilia marker acetylated tubulin (acTUB), and ADP-ribosylation factor-like protein 13B (ARL13B) were also partly visible on the opposing membrane side, indicating very small lumen within the organoid (Fig. 3d and Supplementary Fig. 5). One explanation for the observed PDLO apical-out polarity could be the lack of extracellular matrix (ECM) deposition in suspension culture format[32–34]. We hypothesize that providing a basement membrane, as mimicked by Matrigel, for the microwell chip-derived PDLOs could facilitate the formation of an epithelium with a strictly apical-inside organization. Indeed, an apical-out to apical-in polarity switch was observed upon transfer of microwell chip-derived PDLOs into a 3D Matrigel culture or after transplantation (Fig. 3d).

Single-cell characterization of duct-like organoids. To reconstruct ductal cell-type development in our microwell chip model and to define time-resolved cell composition according to the transcriptional identity, we performed scRNA-seq analysis of 14,811 cells (Fig. 4a and Supplementary Fig. 6a). Louvain clustering and scRNA-seq data analysis with the two-dimensional data reduction algorithm uniform manifold approximation and projection (UMAP) identified nine cell clusters (Fig. 4b,c). With the progression of the growth factor-induced differentiation process, the

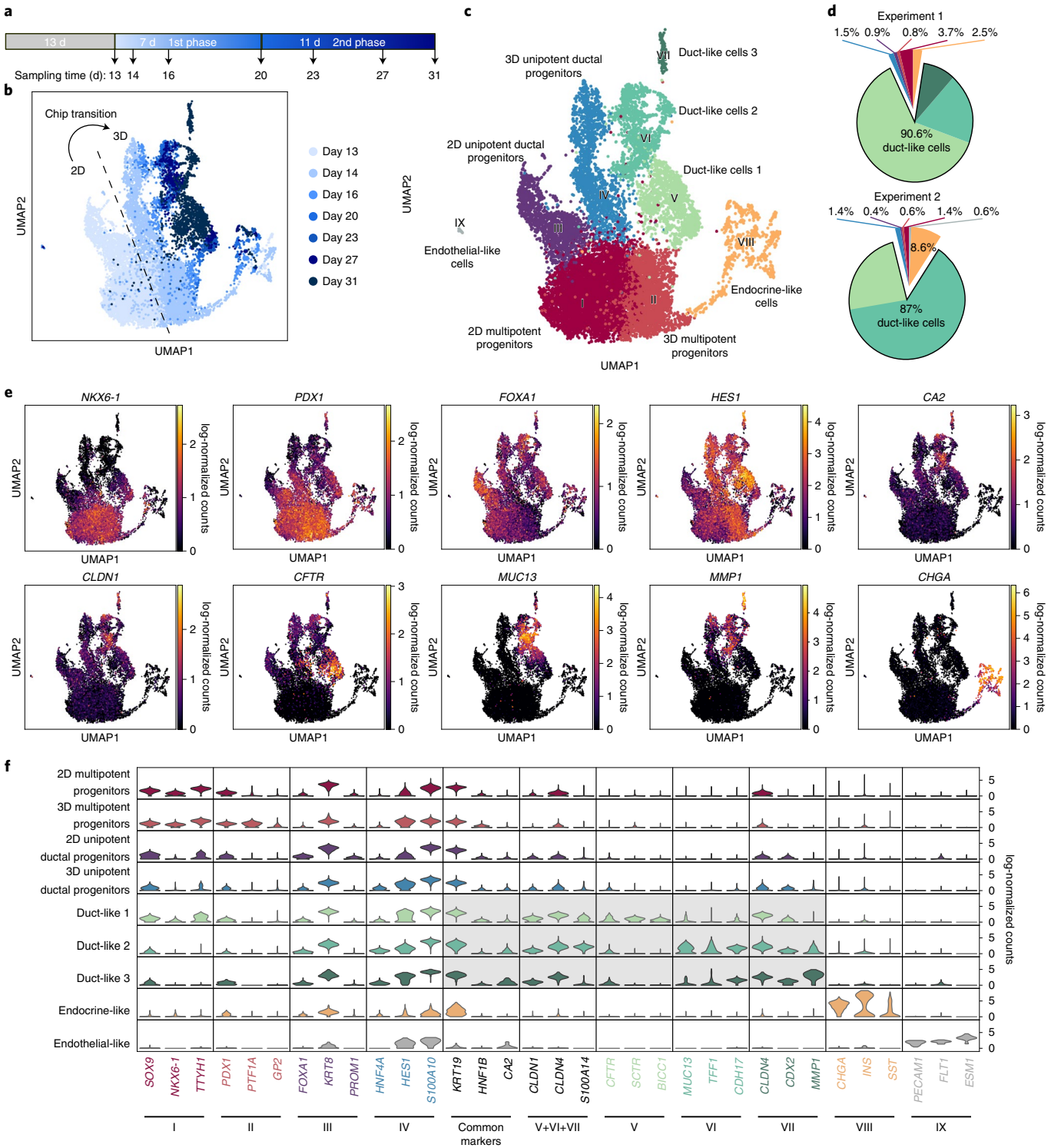

Fig. 4 | scRNA-seq identifies cellular heterogeneity along the differentiation from pancreatic progenitors to PDLOs. a, Schematic representing the sampling time during the ductal differentiation. **b**, UMAP plot of the single-cell transcriptomes recorded along the time course of ductal differentiation. The colours represent the time points of sampling as depicted in **a**. **c**, UMAP cell-cluster representation of the scRNA-seq data. Nine unique cell clusters were identified during the ductal differentiation. **d**, Cell-type distribution at the end point of two independent ductal differentiation experiments. **e**, Expression patterns of selected cell marker genes used for pancreatic cluster assignments. Further marker genes are depicted in Supplementary Fig. 7a. **f**, Violin plot shows mRNA expression levels of DEGs specific to one of the nine cell clusters and commonly used pancreatic ductal markers as indicated below the graph.

recorded single-cell transcriptomes changed substantially, indicated by the time-dependent emergence of the distinct cell clusters (Fig. 4b). All cell clusters could be assigned to cell types by matching known pancreatic developmental genes to the differentially expressed genes (DEGs) in the respective cluster, including three duct-like clusters (Fig. 4c–e and Supplementary Data 1). To test the

robustness of the differentiation approach on the single-cell level, we sequenced the end stages of two independent experiments. In both cases, approximately 90% of pancreatic progenitors developed into cells with a transcriptomic profile of one of the duct-like clusters (Fig. 4d). Violin plots highlight a selection of DEGs specific for each cluster (Fig. 4f). The major cell populations identified included four presumptive progenitor cell types (clusters I–IV), three types of duct-like cells (clusters V–VII), a small endocrine-like cell population (cluster VIII) and a subset of non-pancreatic cells, namely endothelial-like cells (cluster IX). Intriguingly, our starting pancreatic-progenitor-cell population, which was generated in a 2D cell culture, contained cells with different transcriptional profiles suggestive of multipotent and unipotent ductal progenitor cells. In both cell clusters, common progenitor markers were expressed, including *PDX1*, *HNF1B* and *SOX9* (Fig. 4e,f and Supplementary Fig. 6c). Cluster III, hereafter designated unipotent ductal progenitors (UDPs), showed high expression of *KRT8* and low expression of *NKX6-1*, suggesting that these cells committed to a ductal-primed fate at the end of the 2D cell differentiation[35,36] at day 13. Upon aggregation of the 2D cultured progenitors on microwell chips, both corresponding 3D progenitor clusters were transcriptionally re-identified; however, a subset of pancreatic-progenitor markers showed specific alteration patterns (Fig. 4b,f): 3D UDPs (cluster IV) upregulated the markers HES family bHLH transcription factor 1 (*HES1*) and S100 calcium-binding protein A10 (*S100A10*), whereas cluster II showed an increased expression of glycoprotein 2 (*GP2*) and pancreas-associated transcription factor 1a (*PTF1A*), which were specific to this subpopulation (Fig. 4f and Supplementary Fig. 6c). *PTF1A* and *NKX6-1* were co-expressed only in cluster II, suggestive of multipotent pancreatic progenitors (MPPs), which can give rise to acinar, endocrine and ductal cells in mice[37,38]. With the progression of differentiation, three duct-like cell clusters emerged, characterized by high *KRT19* and *SOX9* and intermediate *CA2* expression; the latter being a hallmark enzyme of mature pancreatic ducts[39] (Fig. 4f and Supplementary Fig. 6c). Differential gene expression of the combined three duct-like clusters revealed significant upregulation of ductal epithelial markers such as *CLDN1* and *S100A14*. While duct-like 1 cells specifically expressed HCO_3^- secretion-related proteins such as CFTR, duct-like 2 cells were enriched for mucin-related genes; for example, *MUC13* and trefoil factor 1 (*TFF1*). The duct-like 3 cluster contained only 134 cells and showed similarities to duct-like 2 cluster with significantly higher expression of *CLDN4* and *MMP1*. We also resolved a small fraction of endothelial cells and pancreatic endocrine cells. Doubling the initial cell number of the pancreatic-progenitor aggregates did not influence the outcome of the ductal differentiation (Supplementary Fig. 6b).

Ductal cell subpopulations in PDLOs. To validate duct-like cell types identified in single-cell transcriptomics on a protein level, we performed immunofluorescent staining for specific cluster markers on microwell chip-derived PDLOs. We stained PDLOs differentiated on our microwell chip to day 23, 27 and 31 for CFTR and MUC13. CFTR was expressed only in cells of multi-layered epithelial PDLOs, and MUC13 was expressed in a different subset of cells at the outer side of multi-layered epithelial and in all cystic PDLOs (Fig. 5a,b). A differential expression pattern of a mucin-rich ($MUC1^+$) and a $CFTR^+$ ductal subtype within the pancreas has been reported previously[24]. While MUC1 transcripts were not detected in the PDLO scRNA-seq data, MUC1 protein expression was readily found by immunostaining and label-free mass spectrometry on bulk PDLOs (Fig. 5b, Supplementary Fig. 7a and Supplementary Data 4). Next, we performed combinatorial staining of PDLOs for further proteins encoded by duct-like subcluster DEGs. Indeed, we found distinct expression patterns and fluorescence intensities across multi-layered epithelial PDLOs for MUC1, CFTR, BICC1, MMP1 and TFF1 (Fig. 5b and Supplementary Fig. 7a). For instance, BICC1 was broadly detected but often appeared weaker in MUC1-positive cells. In larger PDLOs, MMP1 was localized to the peripheral layers, while CFTR also appeared in luminal structures inside the organoid (Fig. 5b and Supplementary Fig. 7a). Overall, protein expression of the scRNA-seq based duct-like subtype markers were not mutually exclusive, in agreement with the single-cell transcriptomic data (Fig. 4e,f).

To translate these spatial expression patterns from microwell chip-derived PDLOs to primary human pancreatic tissue, we stained healthy pancreata and a chronic pancreatitis specimen for the cluster-specific markers (Fig. 5c,d and Supplementary Fig. 7b,c). MUC1 was restricted to acinar structures, centroacinar cells and connected intercalated ducts; the connected intercalated ducts also expressed CFTR (Fig. 5c, first and second row and Supplementary Fig. 7b). We also stained KRT19, confirming ductal identity. The marker pattern changed according to the size of the branching ducts, indicating a transition between different co-expression patterns. For example, CFTR expression decreased in intralobular ducts and was hardly expressed in larger ducts, where BICC1 became more prominent (Fig. 5c, third row). In addition, BICC1 was rarely detected in cells in direct proximity to the MUC1-positive cells. Conversely, MMP1 was essentially absent in intercalated ducts but showed a variable staining intensity within larger ductal structures (Fig. 5c, fourth row and Supplementary Fig. 7b). MUC13, TFF1 and SCTR could not be detected in healthy ducts (Fig. 5c, fifth row and Supplementary Fig. 7b). Immunostaining of chronic pancreatitis tissue further confirmed duct specificity, exhibiting differential expression patterns of the described markers and revealing SCTR expression in metaplastic ductal epithelium (Fig. 5d and Supplementary Fig. 7c). Together, these data demonstrate spatially changing expression patterns of the ductal cell-type markers MUC1, CFTR, BICC1, MMP1, TFF1 and SCTR at protein level in PDLOs and in human primary tissue. Thus, expression states are probably more dynamic and complex than the initial transcriptomic subgrouping had suggested.

Trajectory of the in vitro ductal development. To resolve time-dependent relationships during PDLO differentiation, we performed dynamic RNA velocity analysis[40,41]. First, we calculated a latent time on the basis of the balance of spliced and unspliced RNA transcripts within the single-cell transcriptomes (Fig. 6a). Indeed, the theoretical latent time matched true chronological differentiation times (compare with Fig. 4a). The corresponding RNA velocity streamlines indicate two differentiation routes from pancreatic progenitors towards duct-like cells: (1) duct-like 1 cells evolved from MPPs, and (2) duct-like 2 cells mainly evolved from UDPs, which were already present at the pancreatic-progenitor stage (Fig. 6b). Velocity streamlines also directed from duct-like 1 to duct-like 2 cells, indicating a relevant degree of plasticity as reported previously in the pancreas[42]. Few endocrine cells emerged from the MPP cell cluster. Consistent with the velocity analysis, partition-based graph abstraction analysis showed a connectivity (edges) between clusters (dots) along the second ductal differentiation route (Fig. 6c). Evaluation of cell cycle states showed that maturation of duct-like cells was accompanied by a gradually decreasing fraction of cells in G2 and S phase (Fig. 6d). Subsequently, we plotted the changes in the expression of common stage-specific markers along the latent time to trace ductal differentiation. In line with mouse development data, expression of pancreatic-progenitor markers including *GP2*, tweety family member 1 (*TTYH1*), *PDX1* and *PTF1A* decreased over time. Conversely, ductal markers such as *S100A14*, *CFTR*, *TFF1* and *CA2* were upregulated (Fig. 6e). Concordance between transcriptional dynamics of MPP markers and genes that are essential during mitosis (topoisomerase 2 (*TOP2*) and cyclin B2 (*CCNB2*)) was observed, all of which decreased in level during the differentiation process

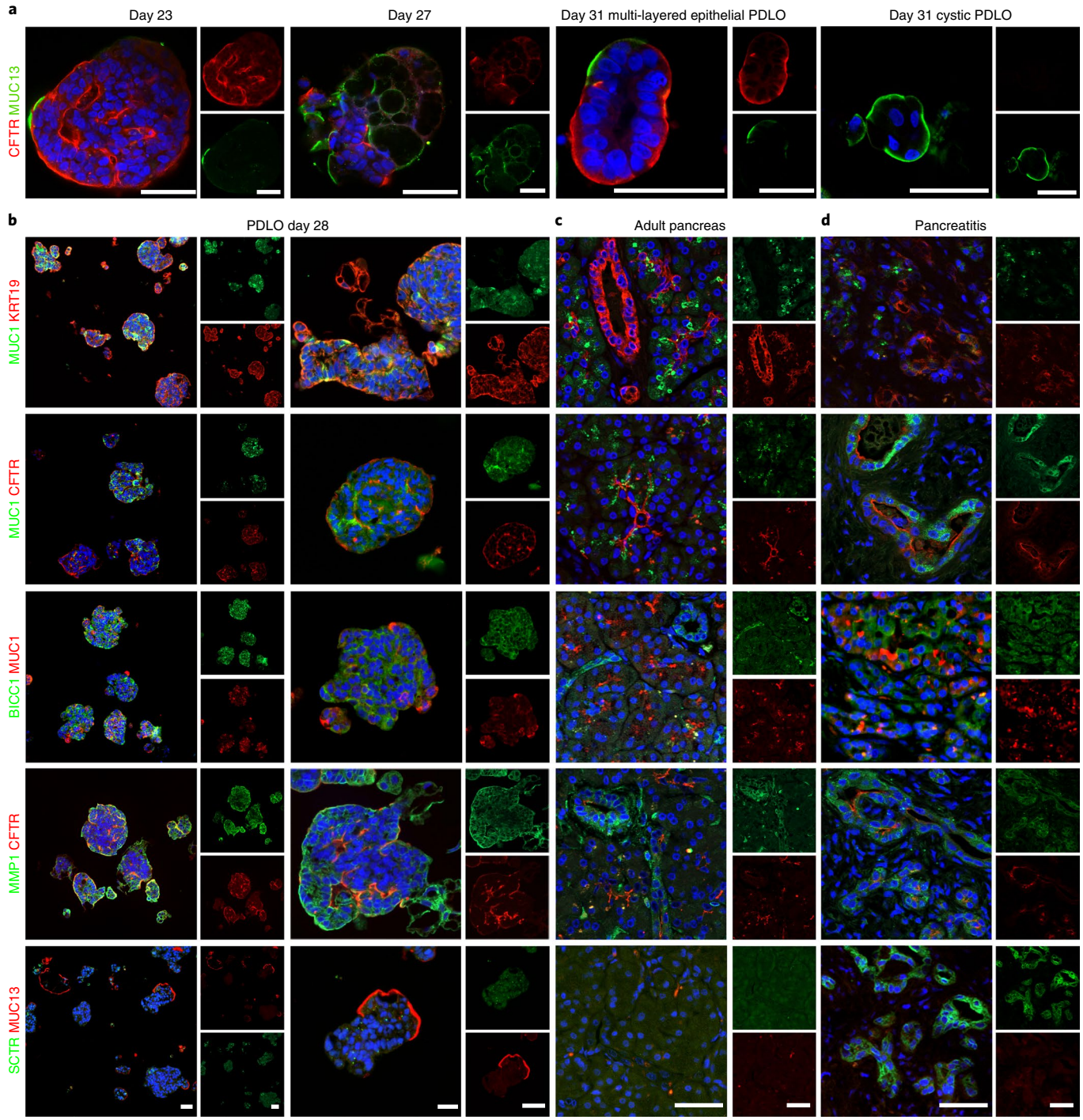

Fig. 5 | Ductal subcluster-specific genes located within PLDOs and primary pancreas tissue on the protein level. a, PDLOs after 23, 27 and 31 DOD were stained for duct-like cluster 1 marker CFTR and duct-like cluster 2 marker MUC13. **b**, PDLOs differentiated until day 28 stained for cell subtype markers identified by the scRNA-seq analysis. **c**,**d**, The same markers are used to locate the in vitro-generated duct-like cell subtypes in primary human healthy pancreas (**c**) or pancreatitis (**d**) tissue. Complementary images are presented in Supplementary Fig. 7. Scale bars, 50 µm.

(Fig. 6f). The top 300 dynamic genes are listed in Supplementary Data 2. Upon ductal cell fate commitment, genes characteristic for pancreatic secretion (*CFTR* and *SCTR*) were transiently induced, accompanied by gradual increases in genes involved in mineral absorption (metallothionein 1E (*MT1E*)). Further, *MUC13* was upregulated, showing a similar temporal expression profile as genes associated with lipid transport or metabolism (apoliprotein B (*APOB*)) and genes less studied in the pancreatic duct such as *TFF3* or macrophage stimulating 1 (MST1), the latter being critical for maintaining exocrine differentiation status and tissue integrity[43]. Since we also detected dynamical expression of several ECM-related genes, we analysed the scRNA-seq data in more detail regarding changes in expression of ECM components during PDLO maturation. Duct-like cells increased the expression of laminin-α3 and -α5 subunits (Supplementary Fig. 8a). At the same time, corresponding laminin-binding integrins were expressed, supporting

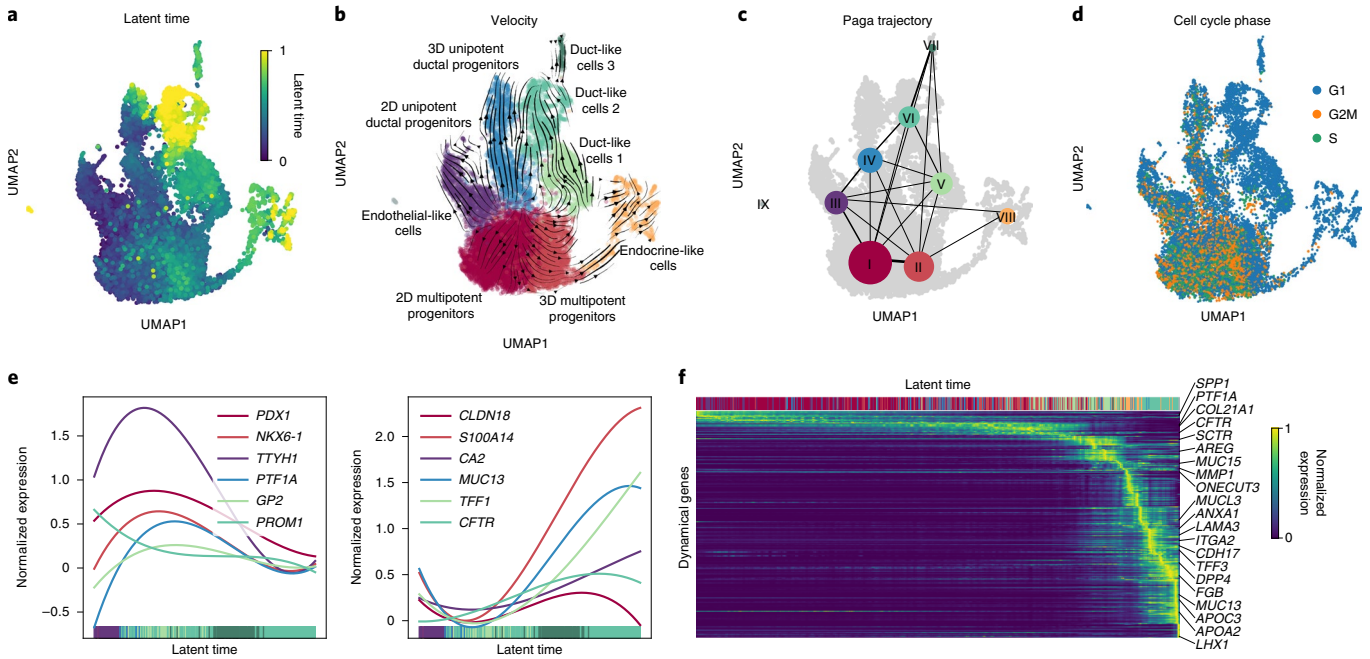

Fig. 6 | Recovery of transcriptome dynamics predicts differentiation paths for duct-like cell types. a, UMAP cluster plot coloured with the latent time calculated based on dynamic RNA analysis. **b**,**c**, Velocity (**b**) and partition-based graph abstraction (Paga) (**c**) maps reveal the cellular-state progressions during ductal differentiation. Streamlines in **b** indicate the direction of cellular-state changes in the velocity map, and weighted lines in **c** within the graph network indicate higher cell-cluster relations. **d**, UMAP plot highlighting the cell cycle state of differentiating cells. **e**, Gene-expression profiles of progenitor or duct characteristic marker genes along the latent time. **f**, Top 300 dynamical genes sorted accordingly to their likelihood score and cells arranged along latent time.

ECM formation along the differentiation trajectory. Concomitantly, duct-like cells downregulated the expression of basal matrix collagens accompanied by upregulation of collagenases MMP1 and MMP10 (Supplementary Fig. 8b). Pancreatic tubulogenesis requires the basement membrane laminin-1 and an α6-containing integrin receptor for proper initiation, provided by the pancreatic mesenchyme during physiological development[32–34]. Accordingly, progenitor and duct-like cluster 1 cells expressed laminin-α1, duct-like cells 2 and 3 expressed laminin-α3 and laminin-α5 (Supplementary Fig. 8a). Of note, laminin-α4[44] and integrin-α5, which are central for β-cell formation[45], were not expressed in PDLOs or in the progenitor state. By contrast, αVβ5 integrins were upregulated in duct-like cells (Supplementary Fig. 8b), in agreement with previous findings[46]. Thus, PDLOs are likely to secrete soluble ECM and corresponding binding proteins as seen under in vivo conditions. In the open microwell culture format, however, the proteins are most probably resolved in the medium, which would explain the polarity switch of the microwell chip-derived PDLOs upon either in vivo transplantation or 3D Matrigel culture (Fig. 3d).

In addition to the ECM genes, we integrated a set of signalling pathways related to the applied growth factor stimuli and found that EGF- and FGF10-mediated MAPK–ERK and ErbB signalling peaked in the duct-like clusters 1 and 2. Compatibly, charting gene signatures representative for processes occurring in mature ducts such as pancreatic secretion or mucin type *O*-glycan biosynthesis further supports that duct-like cells were generated on the microwell chip (Supplementary Fig. 9a–d).

***CFTR*⁺ and *mucin*⁺ subpopulations in primary duct tissue.** One demand for the microwell chip-derived PDLOs is that the duct-like cell types closely resemble human tissue; we therefore integrated three scRNA-seq datasets from primary human pancreas tissue[23,24,26] into our PDLO differentiation kinetics (Fig. 7a). Within the re-clustered combined dataset, duct-like clusters from PDLOs mapped with primary duct cells. Ductal progenitors from the in vitro differentiation trajectory clustered separately, as did endocrine, acinar and endothelial cells. A comparison of the initial cell-type assignments with the cluster location in the combined dataset further substantiated the integration approach (Fig. 7b). Previous reference data from primary ducts described two ductal cell types[24]—one expressing *MUC1* or *TFF1* and a second with *CFTR* as the cluster marker gene. Highlighting *CFTR* and *TFF1* within the combined dataset confirmed the presence of ductal cell subtypes in the PDLOs (Fig. 7a and Supplementary Data 3). In fact, PDLO cells positive for *CFTR* clustered with the primary *CFTR* duct cell type, and PDLO cells positive for *MUC13* or *TFF1* clustered with primary *MUC1* or *TFF1* duct cells. Data integration can lead to an overinterpretation of cell-type similarities. To confirm our ductal cell subpopulation analysis without data integration, we re-clustered the largest primary human ductal single-cell dataset (Supplementary Fig. 10a,b) and searched for our cluster markers[21] (Supplementary Fig. 10c–e). Indeed, the duct-like 1 cluster markers *CFTR, BICC1* and *SCTR* were expressed in cell clusters separated from the duct-like 2 and 3 cluster markers *MMP1* and *TFF1* (Supplementary Fig. 10d,e). In addition, we calculated a gene-expression enrichment score of the top 100 DEGs of the primary *CFTR*⁺ and *MUC1*⁺ duct subpopulations from Baron et al.[24] across the PDLO differentiation kinetics. *CFTR*⁺ and *MUC13*⁺ PDLO cells again correlated with the corresponding primary ductal subpopulations (Fig. 7c). In summary, both primary ductal cell subtypes could be found with a similar scRNA-seq expression pattern in vitro using the microwell chip technology.

Applications of the microwell chip. The microwell chip could be used for various applications. One example was for the investigation of cell–cell communication between pancreatic ducts

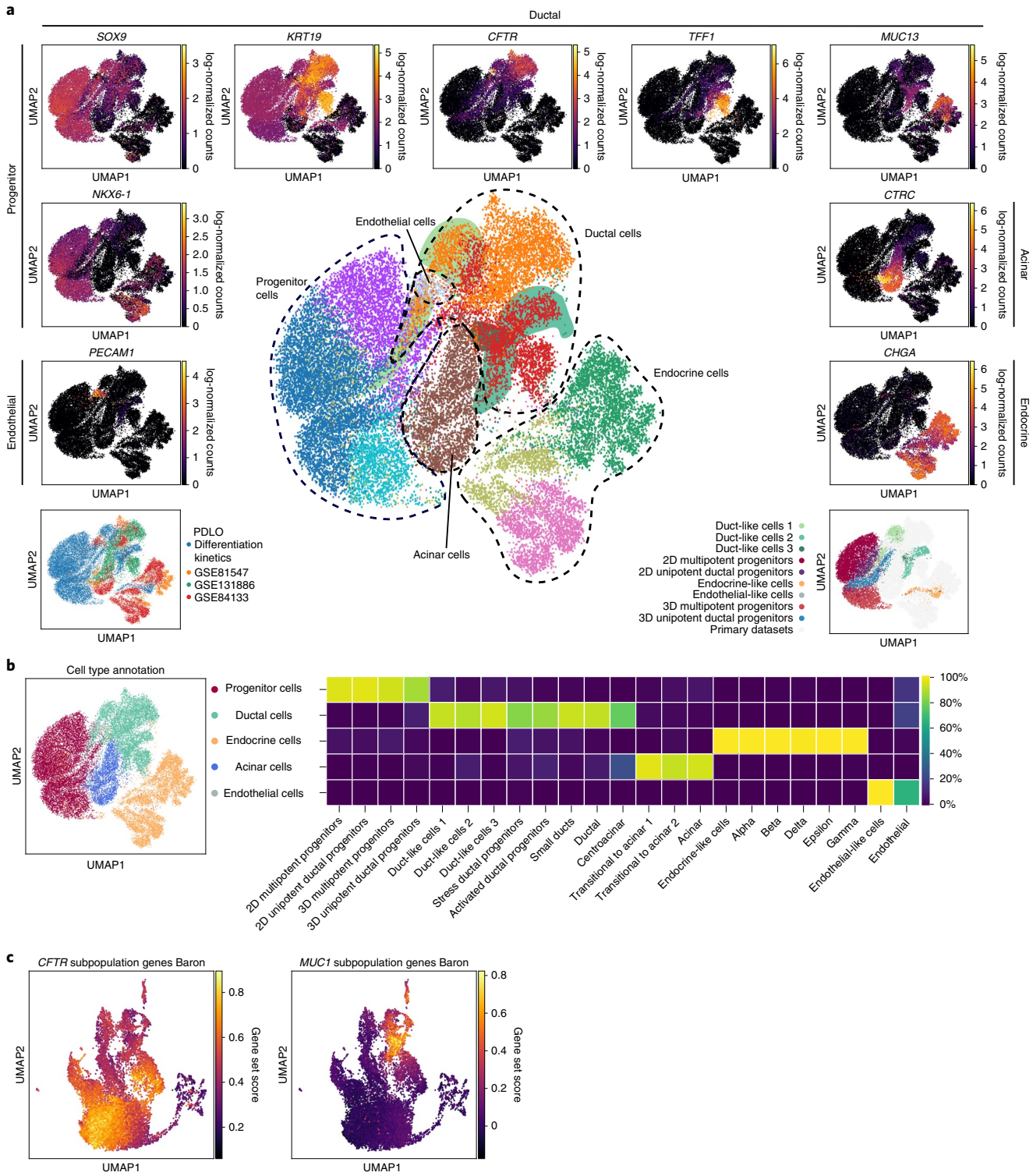

Fig. 7 | Duct-like cells of the PDLOs clustered with primary ductal cells and resembled *CFTR*$^+$-/mucin$^+$-subpopulations. a, Integration of three primary pancreas scRNA-seq datasets[23,24,26] (bottom left) into 10 Louvain clusters (middle plot, duct-like PDLO cells are highlighted by areas in their cluster colour). UMAP expression plots display cell-type-specific marker gene expression (surrounding graphs). Bottom right illustrates the location of our PDLO differentiation kinetics. Analysis of the *CFTR*$^+$/*mucin*$^+$ subpopulations in the isolated scRNA-seq dataset of Qadir et al.[26] is shown in Supplementary Fig. 10. **b**, Annotated cell types with their percentile distribution of the original clusters. **c**, Enriched expression of the marker genes for the *CFTR* high/*MUC1* low and *MUC1* high/*CFTR* low subpopulations defined in Baron et al.[24] during PDLO differentiation.

and various types of stromal cells. Four fluidic separable hexagonal arrays on the microwell chip were exploited to establish a cross-contamination-free co-culture of PDLOs and human pancreatic stellate cells (HPaSteCs) (Supplementary Fig. 11a). The latter resemble quiescent stromal cells in the pancreas able to convert during inflammation, injury or cancer development to a

metabolically active state via auto- and paracrine signals, then serving as a central player in the pathogenesis of pancreatic disease[47]. Quantitative proteomic analysis of PDLOs and HPaSteCs separated co-cultured cells from their individually cultured counterparts (Supplementary Fig. 11b). None of the high-abundance proteins of the individual cultured HPaSteCs and only 2% of those of the PDLOs were found in the upregulated protein set of the co-cultured PDLOs and HPaSteCs, which suggests that there was negligible cross-contamination on the microwell chip (Supplementary Fig. 11c). Enrichment for similar Gene Ontology (GO) terms indicated reciprocal signalling between the two cell types. Pathways involved in energy metabolism and cellular signalling were enriched in co-cultures compared with single cultures (Supplementary Fig. 11c). An in silico constructed protein network in co-cultured PDLOs and HPaSteCs resembled a mitogenic pattern in support of metabolic activation[47] (Supplementary Fig. 11d).

Another application of the microwell chip is the discovery of prognosticators and/or early-stage pancreatic cancer biomarkers. Secretomes derived from either wild-type or genetically modified pancreatic ducts could be a promising resource and the open accessibility of microwells enabled their characterization from the hydrogel-free environment of the PDLOs by collecting the supernatant. To obtain sufficient protein, we made use of label-free mass spectrometry and upscaled the microwell chip to 1,196 PDLOs (Fig. 8a). Mass spectrometry identified 2,528 secreted proteins with high confidence level (Supplementary Data 4), retrieved over a time interval of 8 h, out of which 167 contained a signal peptide for active secretion into the extracellular space[48]. GO-term analysis of the PDLO secretome showed an enrichment of enzymes with hydrolytic and lipid-binding function (Fig. 8b). Scoring the filtered secretome against all human tissue types revealed significant enrichment for the term 'pancreas, glandular cells' (Fig. 8b). Finally, we used the secretome and scRNA-seq data to identify potential prognostic markers of PDAC by using our microwell technology. Within the top 200 DEGs of the duct-like clusters and the 2,528 proteins of the filtered PDLO secretome, 30 and 186 unfavourable prognostic markers for pancreatic cancer[49] were found, respectively (Fig. 8c). Eleven of the transcriptomic proteins and 38 of the markers identified in the secretome were predominantly expressed in pancreatic duct cells.

Filamin b expression in human pancreatic cancer cohorts. One unfavourable PDAC marker in the overlapping protein set was filamin B (FLNB), which has been identified in a secretome screen from pancreatic cancer cell lines without validation in human patients[50] (Fig. 8d). FLNB exerts tissue- and context-dependent functions in distinct cancers, whereas both gain and loss of function have been shown to foster cancerous properties[51,52]. To investigate FLNB expression during pancreatic carcinogenesis[53], we assessed FLNB protein expression in an independent cohort of resected PDACs[54–56] by immunohistochemistry (Fig. 8e). Normal pancreatic ductal epithelium and some acinar glands were faintly FLNB positive at their luminal surface. As expected, microwell chip-derived PDLOs were also FLNB positive (Fig. 8e and Supplementary Fig. 12a,b). By contrast, PDAC strongly expressed FLNB in the cytoplasm and on the entire cell surface in concordance with the loss of polarity in the carcinoma cells (Fig. 8e and Supplementary Fig. 12b). Immunohistochemical observation was specified using the semi-quantitative H-score method followed by correlation with clinical data[57]. Comparing normal ductal epithelium with corresponding cancer tissue revealed significantly higher H-scores in PDAC (Fig. 8f), whereas H-scores did not correlate with any clinical parameter including survival (Fig. 8g). Pancreatic intraepithelial neoplasias (PanIN) represent the most relevant PDAC precursor lesions and can be frequently found adjacent to PDAC and their presence is of prognostic relevance[58–60]. Interestingly, H-scores were also elevated in PanINs compared with normal ducts (Fig. 8f). FLNB expression in PanIN lesions significantly correlated with increased survival of patients (modifed overall survival; $P=0.0019$) (Fig. 8g and Supplementary Fig. 12c). A gradual increase from normal to preneoplastic lesions has been described, for example, for the epigenetic silencer enhancer of zeste homologue 2 (EZH2)—in established cancers, higher expression levels were associated with better prognosis[61]. As alternative splicing can lead to shorter FLNB isoforms being strongly associated with gene signatures of epithelial–mesenchymal transition in basal-like breast cancer patient samples, distinct forms might also be present in pancreatic cancer precursor lesions, leading to distinct biological outcomes[62]. To probe the feasibility of FLNB as a biomarker for liquid biopsy, we consulted an independent cohort of human patients with metastatic PDAC and measured FLNB levels in peripheral blood. When comparing FLNB levels in peripheral blood, no obvious differences were observed between patients with metastatic PDAC and healthy volunteers; however, metastatic samples clustered into two FLNB groups. To dissect this clustering in more detail, we correlated clinical and histological characteristics of the PDAC patients with individual FLNB levels in peripheral blood. Intriguingly, differentiated tumours (grade 2 or less) had significantly higher FLNB peripheral blood levels when compared to less differentiated tumours (grade 3 or more) or healthy donors, the latter two sample sets having more or less similar levels (Fig. 8h). We conclude that FLNB might be a suitable blood biomarker for differentiated PDACs and could therefore complement biomarker panels detecting early PDAC formation or discriminating differentiated and dedifferentiated PDAC.

Discussion

We have developed a microwell chip to engineer PDLOs from hiPSCs, and charted their cellular heterogeneity during the differentiation trajectory. The advances of the microwell chip are (1) the low consumption of cells and materials, (2) defined and homogeneous size of generated 3D aggregates, (3) the possibility for long-term 3D cell culture, (4) sample retrieval for downstream analysis with

Fig. 8 | Potential PDAC biomarkers in the secretome and transcriptome of PDLOs. a, Microwell chip used for the determination of the PDLO secretome by LC–MS/MS of three biological replicates, with one, two and five technical replicates, respectively. **b**, Left: filter process applied to the secretome data. Right: GO terms enriched within the filtered PDLO secretome with relevance for ductal function. LDL, low-density lipoprotein. **c**, Prognostic pancreatic cancer markers within the top 200 DEGs of the combined duct-like clusters from the scRNA-seq analysis and within the PDLO secretome. The Venn diagram highlights the overlap between the revealed unfavourable diagnostic markers for pancreatic cancer from the scRNA-seq and secretome analysis. Pancreatic duct expression was assessed by examination of Human Protein Atlas staining[77]. **d**, Literature survey for the set of unfavourable diagnostic markers from the table in **c**. The chart shows the number of markers, with examples. **e**, Immunohistochemistry staining of FLNB in PDAC tissue. Purple arrows indicate PDAC, orange arrows show PanINs and green arrows point to healthy ducts. Scale bar, 50 µm. Complementary images are shown in Supplementary Fig. 12. **f**, Mean FLNB H-score in heathy, ($n=86$), PanIN ($n=28$) and PDAC ($n=84$) tissue. Error bars denote standard deviation. The Mann–Whitney *U*-test was applied to calculate statistical significance. **g**, Overall survival curve for patients with high and low FLNB H-score. High FLNB H-scores in PanINs correlated with a favourable prognosis for patients. *P*-value was calculated with the log-rank test. **h**, Median FLNB blood concentration in a healthy control group ($n=11$) and patients with PDAC grade ≤2 ($n=10$) and ≥3 ($n=7$). The Mann–Whitney *U*-test was used to calculate statistical significance. $^{*}P<0.05$, $^{**}P<0.01$, $^{***}P<0.001$. NS, not significant.

minimal perturbation, and (5) the possibility to establish co-cultures. We challenged the potential of this microwell chip for application and comprehensively analysed the secretome and proteome to identify potential prognostic and diagnostic PDAC biomarkers.

Microwell culture is a low-cost cell culture technology offering uniformity for the aggregation process and flexibility in design for multiple downstream applications. The microwell chip implements 3D pancreatic-progenitor aggregates to generate two morphologically

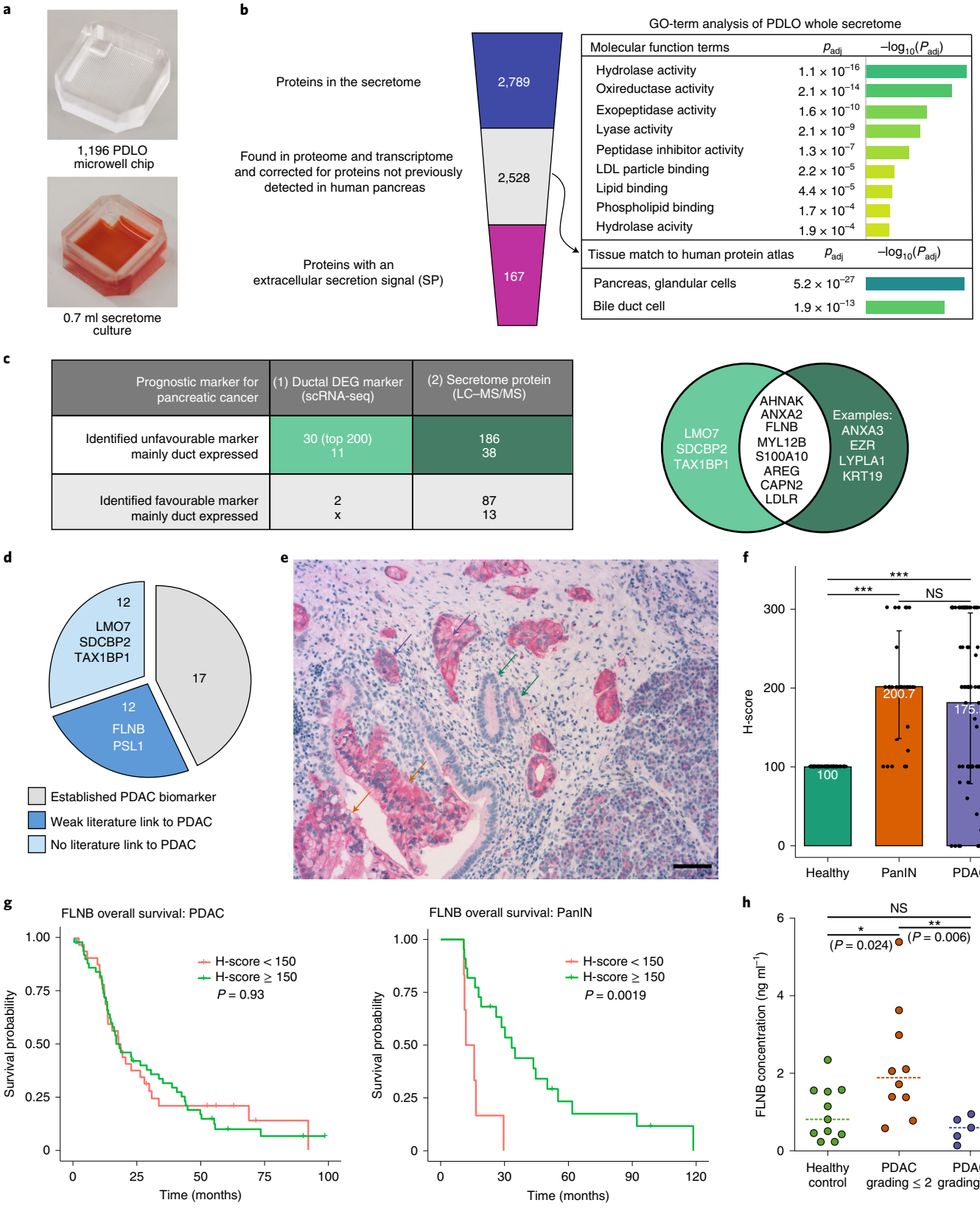

distinct PDLO types: a multi-layered epithelial type and a cystic PDLO type. Pancreatic organoids generated from healthy or cancerous human pancreata grown in hydrogels show cystic morphologies[7,12,63], with an apical-in polarity. By contrast, microwell chip-derived PDLOs exhibited predominantly, but not entirely, apical-out polarity. After engraftment in mice, they formed ductal structures exhibiting their apical side to the lumen. The same switch to apical-in polarity was found when PDLOs were transferred from the microwell chip to an embedding laminin-rich hydrogel culture as mimicked by Matrigel. This indicates that ECM components are also involved in the induction of ductal epithelial polarity. The inversion of apical-in to apical-out cell polarity upon transferring organoids from hydrogel to suspension cultures has been previously described for enteroids[64]. The dominant apical-out conformation of PDLOs enhances constant exposure to external stimuli, allows easy access to the secretome of cells, and makes the apical membrane accessible for various studies, such as the study of membrane barrier functions or pathogen infections. Nevertheless, swelling in cystic PDLOs upon stimulation with forskolin suggests a relevant degree of luminal CFTR activity at the inner membrane of PDLOs.

PDLO development in microwells also facilitates the stepwise study of synchronous human duct development. Time-resolved single-cell transcriptomics characterized the entire cell populations evolving from the pancreatic progenitor to duct-like cell stage. Interestingly, the duct-like cells differentiated on microwells clustered together with three reference primary duct cell types in published scRNA-seq datasets and could be stained in primary human pancreas tissue. Furthermore, counterparts of the previously identified ductal cell subtypes in the adult pancreas with mucosal restitution (*MUC1*) and HCO_3^- secretion (*CFTR*) transcriptomic profile[24] were identified within the in vitro-generated PDLOs. Besides ductal heterogeneity at terminal differentiation stages, emerging intermediates revealed important details about ductal cell-type commitment. Hitherto, it has been suggested that endocrine precursors delaminate from a common trunk domain arising at embryonic day 12.5 in mice, which further undergoes tubular morphogenesis to subsequently form the ductal network[38]. Although the timing of particular marker expression is slightly different, detection of similar markers suggests the presence of a trunk and tip domain during human pancreas development[19,38]. An unexpected finding of our analysis was the lack of a trunk domain subcluster, at least based on the in vitro marker gene analysis. Velocity analysis suggests that the microwell-derived duct cell types generated from distinct temporarily co-existing progenitor populations harboured distinct potency. The few endocrine cells present in PDLOs evolved from the 3D MPPs, which were positive for classical tripotent pancreatic-progenitor labels, including *GP2* and *PTF1A*, contradicting a trunk-like state[18]. We did not detect a PTF1A$^-$/NKX6.1$^+$ cell cluster in close proximity to endocrine and ductal cells that would represent an intermediate population giving rise to those two lineages. Possible explanations for the absence of such a trunk domain—as described in mouse development[18]—could be an early ductal priming of PDLOs or insufficient scRNA-seq sampling time intervals. By contrast, *MUC13*-positive ductal cells evolved from UDPs, being present at day 13, and to a smaller extent, from the *CFTR*-positive duct cell type. We cannot exclude that the applied chemical induction protocol does not entirely resemble the in vivo development of the pancreas, and that artificial aberrations of the trunk model are induced. Differences between in vitro and in vivo progenitors have been observed during endocrine development, which also did not report a distinct trunk-like stage[65–67]. Additional developmental routes of pancreatic progenitors have been postulated from in vivo mouse scRNA-seq data[68], and the development of a ductal subpopulation from *Pdx1*$^+$/*Ptf1a*$^-$ pancreatic-progenitor cells has been directly demonstrated in vivo by lineage tracing experiments[69,70]. Thus, it appears that the heterogeneity of pancreatic progenitors is larger than expected. Only single-cell data of primary human ductal embryonic development, which we currently lack, could further refine the in vitro PDLO engineering approach. Our finding that *CFTR*$^+$/*mucin*$^+$ duct-like cell types in the PDLOs resemble primary adult human duct cells indicates that PDLOs can be applicable for modelling diseases of the pancreatic ductal compartment, especially pancreatic cancer.

There is currently no efficient screening approach for early tumour detection. Personalized treatment of pancreatic cancer is still in its infancy, and predictive biomarkers are largely missing. Thus, secreted biomarkers from early neoplastic ducts could overcome this lingering unsolved obstacle. In this regard, the microwell chip can be a central interface tool for analytical methodologies such as mass spectrometry. PDLOs expressing oncogenic driver genes and probed on our microwell chip could serve as a hub to dissect oncogene-specific secretomes. Our data provide a proof of concept by determining the secretome of the genetically unaltered PDLOs and implementation of a systematic downstream biomarker classification, which we use to investigate potential diagnostic and prognostic pancreatic cancer markers against a comprehensive PDAC biobank.

Methods

Microwell chips. All microwell chips used within this study consisted of four hexagonal microwell arrays surrounded by 12 pillars. Each pillar had a diameter of 0.6 mm and a height of 4 mm. The three different microwell chips had well diameters of 150 µm, 300 µm and 600 µm with 251, 61 and 19 wells per array, respectively. The well diameter:well depth ratio on each microwell chip was 1:1.5. For visualization, the 3D print model of the 600 µm microwell chip is displayed in Fig. 1a.

Moulds of the PDMS microwell chips were printed using the Freeprint mould (Detax) resin in a SLA 3D printer (Asiga PICO2 HD 27) with a slice thickness of 10 µm. After washing the prints twice with isopropanol for 10 min, moulds were incubated at 80 °C for 1 h. Post-curing of the parts was achieved with an Otoflash G171 (NK-Optik) unit by exposing each side of the mould to 2,000 flashes under nitrogen environment. To ensure complete evaporation of isopropanol, moulds were incubated at 80 °C overnight.

PDMS microwell chips were produced by standard soft lithography. In short, 3D printed moulds were precoated with 0.1% hydroxypropylmethylcellulose (Fluka Analytical) dissolved in 0.2 M sodium phosphate (Sigma) (pH 3, adjusted with 0.1 M citric acid (Sigma)) for 10 min, based on the method of Gitlin et al.[71]. The 3D-printed moulds were washed with deionized water and dried with nitrogen. 1:10 PDMS (SYLGARD 184 Silicone Elastomer Kit, Dow Chemical Company) was cast and degassed in a vacuum chamber. A glass substrate was placed onto the microwell chip spacer structures and the PDMS was cured for 1.5 h at 80 °C.

Cell seeding onto the microwell chip technology. Before cell seeding, microwell chips were coated with 10% Pluronic F-127 (Sigma) overnight and sterilized for 30 min using 254 nm UV light (NK-Optik). On the next day, microwell chips were washed twice with Dulbecco's Phosphate Buffered Saline (PBS) (Gibco) and once with DMEM:F12 (Gibco). For ductal differentiation on microwell chips, pancreatic progenitors were washed with PBS, then incubated for 3–8 min with TrypLE Select (Gibco) at 37 °C for detachment. Pancreatic progenitors were centrifuged at 200*g* for 5 min and then seeded in 35 µl PDLO medium per array. The surface tension on top of the arrays allowed an equal distribution of the cell-suspension. After cell settling at 37 °C for 45 min, additional 660 µl PDLO medium was carefully added to the side of the microwell chip. For preliminary determination of ideal cell numbers for organoid formation, hiPSCs were seeded on the microwell chip in mTeSR1 medium (Stemcell Technologies), supplemented with 10 µM ROCK inhibitor Y-27632 (Abcam) during the first 24 h.

Culture of hiPSCs. Generation and culturing of the hiPSC line has been described previously[14]. In brief, hiPSCs were cultured on hESC Matrigel-precoated plates according to the manufacturer's recommendations (Corning) in mTeSR1 medium at 5% CO_2, 5% O_2, and 37 °C with daily medium change. The general scientific use of the cells was approved by the local ethics committee at Ulm University (reference no. 68/11-UBB/bal.). The exact isolation method, culture and pancreatic differentiation of hiPSCs, and the study of such hiPSC derivatives was approved by the local ethics committee at Ulm University (reference no. 159/19) under informed consent of donors.

HiPSC differentiation to PDLOs. HiPSCs were differentiated into pancreatic progenitors in a monolayer culture based on a fusion protocol from two previously published studies[14,72]. In brief, 2.5×10^5 hiPSCs were seeded in mTeSR1 with

10 µM ROCK inhibitor per well of a 24-well plate, precoated with growth factor reduced (GFR) Matrigel (1:18 in DMEM:F12, Corning). For the first 6 d, cells were differentiated in the backbone media BE1: MCDB131 (Invitrogen) supplemented with 1% Glutamax (Gibco), 0.8 g l^{-1} glucose (Sigma), 1.174 g l^{-1} sodium bicarbonate (Sigma), and 5 g l^{-1} fatty acid free bovine serum albumin (BSA) (Proliant). While 100 ng ml^{-1} Activin A (PeproTech) and 2 µM GSK3β-inhibitor (CHIR99021) (Axon MedChem) were added for 24 h, the medium contained 100 ng ml^{-1} activin A and 5 ng ml^{-1} bFGF (Novoprotein) for the following 2 d. From day 3 until day 6 the BE1 medium was complemented with 50 ng ml^{-1} FGF10 (R&D), 0.75 µM Dorsomorphin (Sigma), and 3 ng ml^{-1} mouse WNT3A (PeproTech). The subsequent backbone medium BE3 was composed of MCDB131, 1% Glutamax, 3.3 g l^{-1} glucose, 1,754 g l^{-1} sodium bicarbonate, 20 g l^{-1} fatty acid free BSA, and 0.5% insulin–transferrin–selenium-X (Gibco). From day 6 until day 9, 50 ng ml^{-1} FGF10, 200 nM LDN-193189, 0.25 µM SANT-1, 2 µM retinoic acid and 0.044 g l^{-1} L-ascorbic acid (all Sigma) were added. From day 9 until day 13, BE3 medium was supplemented with 200 nM LDN-193189, 100 ng ml^{-1} EGF (R&D), 10 mM nicotinamide (Sigma), 330 nM Indolactam V (StemCell Technologies) and 0.044 g l^{-1} L-ascorbic acid. The medium was prepared freshly and changed every day. At day 3 (definitive endoderm), day 9 (pancreatic endoderm) and day 13 (pancreatic-progenitor stage) differentiation efficiencies were analysed by flow cytometry. Pancreatic progenitors were only used when at least 70% of the cells were PDX1 and NKX6-1 double-positive.

For differentiation from pancreatic progenitors to PDLOs, cells were transferred on the microwell chip, facilitating a 3D cell culture. For the first 7 d on the microwell chip, BE3 medium was supplemented with 1% penicillin/streptomycin (Sigma), 10 mM nicotinamide, 10 µM $ZnSO_4$ (Sigma), 50 ng ml^{-1} EGF, 50 ng ml^{-1} FGF10, 50 ng ml^{-1} KGF (PeproTech), 50 nM MSC2530818 (Selleckchem) and 0.044 g l^{-1} L-ascorbic acid (PDLO medium phase I). 10 µM ROCK inhibitor was additionally added for the transfer of pancreatic progenitors on the microwell chip. From day 20 on, cells were differentiated in BE3 containing 1% penicillin/streptomycin, 10 mM nicotinamide, 10 µM $ZnSO_4$, 50 ng ml^{-1} EGF, 50 ng ml^{-1} FGF10 and 0.044 g l^{-1} L-ascorbic acid (PDLO medium phase II). The medium was changed twice a week. The complete differentiation scheme from hiPSCs to PDLOs is shown in Fig. 2a.

Flow cytometry. Differentiation efficiencies were checked on day 3, 9 and 13. The percentage of definitive endoderm cells was assessed by staining the surface marker CXCR4 and c-KIT on day 3. Pancreatic endoderm and pancreatic-progenitor cells were fixed in 4% paraformaldehyde (PFA) (Thermo Fisher Scientific) on days 9 and 13 for intracellular staining of PDX1 and PDX1 + NKX6-1, respectively. Details of the staining procedure have been previously described[14].

Live imaging. For live-cell imaging, PDLOs were imaged from day 24 to 31 of differentiation every 2 h with a Zeiss Axio Observer Z1 microscope. The PDLOs on microwell chip were maintained in cell-culturing conditions with a stage top incubator (Tokai Hit).

Matrigel culture. For studying niche-dependent polarity changes, microwell chip-derived PDLOs were collected and transferred to a Matrigel 3D culture. After pipetting PBS directly on top of the microwells, PDLO cells at day 27 were washed in BE3 medium and PDLOs from one-quarter of the array were resuspended in 50 µl GFR-Matrigel. Domes of 50 µl were seeded on 24-well plate wells and after solidification for 10 min at 37 °C and PDLO medium phase II supplemented with 10 µM Y-27632 was added. After 14 d of culture with medium change (PDLO medium phase II) every 2–3 d, PDLOs were fixed with 4% PFA and 10% sucrose for histological analysis and processed as described in later sections.

Mouse model. NOD *scid* gamma (NSG) mice (NOD.Cg-Prkdc^{scid} Il2rgtm1Wjl/SzJ strain (Charles River); RRID:BCBC_4142) were used for xenotransplantation of PDLOs into the pancreas with permission of the Regierungspräsidium Tübingen (TVA-1406). All animal work was performed under ethical and animal protection regulations of the German animal protection law. Husbandry was performed in standardized hygiene-barrier rooms with reduced pathogen microorganism burden. Female 10-week-old mice were used for xenotransplantation experiments. Housing was performed in groups of two to four mice per cage.

Orthotopic transplantation of PDLOs. Microwell chip-derived PDLOs at day 27 were collected and singularized. After pipetting PBS directly on top of the microwells, cells were washed 2 more times with PBS and singularized with Accutase (Sigma) at 37 °C for 30 min. The enzymatic reaction was neutralized with 1% BSA (Proliant) 1% penicillin/streptomycin (Thermo) in DMEM/F12 (Gibco), cells were washed in BE3 medium and resuspended in PDLO medium phase II supplemented with 20 µM Y-27632 and GFR-Matrigel in a 1:1 ratio. Aliquots with cell–Matrigel mixture were kept on ice until transplantation. Mice were anaesthetized starting 3 d before transplantation by addition of 1 mg ml^{-1} Tramadol (Grünenthal) to the drinking water. To improve the take-up rate when transplanting low numbers of PDLO cells, an acute pancreatitis was induced using caerulein (Sigma). Ten microlitres of a 5 µg ml^{-1} caerulin, 0.9% NaCl solution was injected intraperitoneally every hour 6 times before transplantation. After anaesthesia with isoflurane, a small cutaneous midline incision was followed by a small incision into the peritoneum. A volume of 50 µl with 100,000 cells was injected per mouse directly into the pancreatic tail. Carefully, pancreas and spleen were repositioned in the abdomen before the peritoneum was closed by medical sewing using 5-0 polyglactin coated vicryl suture (Ethicon). Surgical staples were used for closing the skin and removed one week after transplantation, when Tramadol treatment was also stopped. Mice were killed after 8 weeks and pancreata were collected, fixed with 4% PFA at 4 °C overnight, and processed for histological analysis. All animal experiments were performed in compliance with the institutional guidelines, under ethical and animal protection regulations of Ulm University.

Fast acrylamide free tissue clearing and immunofluorescence staining. To enable imaging of whole organoids on microwell chips, the organoids were cleared using a protocol based on fast acrylamide free tissue clearing (FACT)[73]. Organoids were washed once with PBS and then fixed with PFA for 3 d at 4 °C. Washing with PBS was followed by incubation at 37 °C for 1–3 h with 8% ultra-pure SDS (Invitrogen) in PBS for actual clearing. After washing the organoids twice with PBS and PBS-T (0.01% Tween-20 (Roth)), the organoids were blocked and permeabilized with 1% BSA (Roche), 22.52 mg glycine (Roth) and 0.1% Tween-20 for 1 h. The primary antibody was diluted in 1% BSA and 0.1% Tween-20 and samples were stained for 3 d at 4 °C. After washing twice with TBS-T (Duolink), organoids were incubated with the secondary antibody diluted in 1% BSA overnight at 4 °C. The organoids were washed twice with TBS (Duolink) and incubated with 1 µg ml^{-1} DAPI (Sigma) for 15 min. Subsequently, the organoids were washed twice with TBS-T and post-fixed for 30 min with 4% PFA. During confocal imaging (Zeiss Axio Observer LSM 880) the organoids were kept on microwell chips in X-CLARITY Mounting Solution (Logos Biosystems).

Immunofluorescence staining was performed using the following primary antibodies: 1:200 PDX1 (R&D AF2419), 1:200 CDH1 (Cell Signaling 3195), 1:100 KRT19 (Dako M08889), 1:400 and 1:500 SOX9 (Cell Signaling 82630 and Millipore AB5535, respectively), 1:800 CFTR (Cell Signaling 78335), 1:500 MUC13 (BioLegend 363902), 1:200 ZO1 (Invitrogen MA3-39100-A555), 1:500 COL4A1 (Abcam ab6586) and 1:200 CLDN1 (R&D MAB4618). The following secondary antibodies were used: 1:500 anti-rabbit Alexa488 (Invitrogen A21206), 1:2,000 anti-mouse Alexa488 (Invitrogen A21202), 1:1,000 anti-rabbit atto550 (Sigma Aldrich 43328), 1:800 anti-goat Alexa488 (Invitrogen A11055) and 1:800 anti-rat Alexa488 (Invitrogen A21208).

Paraffin embedding of PDLOs. PDLO cultures were collected with PBS as described in the Matrigel culture section. Collection of PDLOs was followed by fixation of PDLOs in 4% PFA with 100 mM sucrose. After incubation at 4 °C overnight, PFA was removed carefully and PDLOs were washed twice with PBS. Samples were pre-embedded in 2% agarose (Sigma) and further processed according to standard histology procedures. After serial dehydration, PDLOs were embedded in paraffin and sectioned at 4 µm. Tissue slices were mounted on SuperFrost Ultra Plus microscope slides (Thermo). Pancreatic tissue from transplantation experiments were fixed, embedded and sectioned as described above without pre-embedding in 2% agarose.

Histological standard techniques. Histological staining, including haematoxylin and eosin staining, was performed according to standard protocols. Paraffin sections of PDLOs or pancreatic tissue were rehydrated in ethanol series followed by either heat-mediated or enzymatic antigen retrieval, depending on the antibody (Supplement Data 6). Commercial Tris buffer (pH 9) or citrate buffer (pH 6, both Vector Laboratories) were used for heat-mediated antigen retrieval in a steamer; a citrate buffer that we made (pH 6, 1.9 g l^{-1} citric acid; Sigma) was used in the pressure cooker. To continue with immunofluorescence staining of paraffin sections, tissue permeabilization was performed with 0.5% Triton X-100/PBS (PBS-T) for 30 min at room temperature. After washing twice, primary antibodies diluted in Antibody Diluent (Zytomed) were added to the slides, which were then incubated overnight at 4 °C in a wet chamber. After washing three times with PBS-T for 5 min, slides were stained with Alexa Fluor secondary antibodies (Thermo) and 500 ng ml^{-1} DAPI diluted in Antibody Diluent for 90 min at room temperature in the dark. Slides where washed three times with PBS-T and finally with dH_2O before sections were mounted with Fluoromount-G (SouthernBiotech).

Immunohistochemistry staining on paraffin tissue sections. Immunohistochemistry staining of FLNB was performed on samples from a comprehensive human PDAC patient cohort consisting of 86 available tissues from resected PDACs[54–56] on a fully automated OMNIS staining device (Dako) using Envision FLEX HRP Magenta high pH kit (Dako, GV900) according to the manufacturer's recommendations. In brief, paraffin slides were incubated with primary FLNB antibody (rabbit, 1:50, Merck, HPA004886) or 30 min at room temperature in a wet chamber, secondary reagent for 10 min, polymer reagent for 20 min and chromogen for 5 min for colour development. Washing steps were performed as described in manufacturer's recommendations. Nuclei were counterstained with 20% haematoxylin (Dako, GC808).

The images were graded according to PDAC and PanIN cells. The intensity of FLNB was denoted from 0 to 3 (0, negative; 3, strongly positive). The percentage of cells with positive FLNB cells within cancerous structures was graded from 1 to 5 (1 denotes 20% and 5 denotes 100% of FLNB-positive cells). All healthy ductal cells were slightly positive and rated 5 for number of positive cells and 1 for intensity.

The H-score[57,74] was calculated by multiplication of intensity scores (intensity of staining) with percentage scores (number of positive cells) in PDAC, PanIN and healthy cells. For the Kaplan–Meier plots, the maximal H-Score per lesion was used for each individual. Individuals who died from non-tumour-related causes were treated as alive. For the bar plot in Fig. 8e a Mann–Whitney *U*-test was used to calculate statistical significance.

Forskolin swelling assay. For the swelling assay, organoids were transferred to a bright-field imaging microwell chip, which was composed of microwells with a diameter of 300 µm and a flat bottom to allow improved bright-field imaging. Cells were stimulated at day 28 with either 20 µM forskolin (Abcam) and 100 µM 3-Isobutyl-1-methylxanthine (Sigma) (forskolin treatment) or 1:1,000 DMSO (control) in DMEM:F12 medium. Live-cell imaging was performed on a Zeiss Axio Observer Z1 microscope for 18 h after treatment. Images of 16 different positions were taken for each sample every 20 min.

Pancreatic stellate cells. Human pancreatic stellate cells (HPaSteCs) isolated from a chronic pancreatitis resection and immortalized by SV40 large T antigen and the catalytic subunit of hTERT[75], were provided by M. Löhr (Karolinska Institute). Cells were cultured in DMEM supplemented with 10% FCS and 1% penicillin/streptomycin and split using 0.05% Trypsin-EDTA (Sigma) twice a week in a 1:6 ratio.

PDLO–stellate co-culture. PDLOs and HPaSteCs were seeded on a fluidic hexagonal microwell chip, facilitating paracrine signalling between PDLOs and HPaSteCs in the same microwell chip without direct cellular contact. For this, 150 cells were seeded per well following the procedure describe above (a schematic is shown in Supplementary Fig. 10a). The PDLOs were derived on the upscaled microwell chip (Fig. 8a), collected at day 31, and transferred onto 2 arrays of the microwell chip (Fig. 1). The microwell chip was filled with phase II ductal media and co-cultured for 3 d without medium change. The 3D HPaSteC aggregates and PDLOs were collected at day 34. Therefore, the media was removed and 40 µl drops of PBS were placed on top of each array. Using surface tension, the HPaSteC aggregates and PDLOs were collected without cross-contamination. They were washed 3 times with PBS with an incubation time of 10 min between washes. The 3D HPaSteCs aggregates and PDLOs were centrifuged at 200*g* for 5 min within the washing steps. The dry pellet was frozen and kept at −80 °C upon sample preparation for proteomic measurements.

PDLO secretome sample preparation for mass spectrometry. To characterize the secretome of PDLOs, an upscaled microwell chip was manufactured. The microwell chip contained 1,196 microwells with a well diameter of 400 µm, a well depth of 600 µm and 600 cells were seeded per well (Fig. 8a). At day 28 of differentiation, PDLOs were washed three times with blank DMEM:F12 medium. Ten minutes of incubation time between the washing steps ensured settling of eventually washed out PDLOs. Then, 700 µl blank DMEM:F12 was added and the supernatant was taken after 8 h for subsequent analysis by mass spectrometry. For the parallel PDLO proteome determination, PDLOs were collected at the end of the experiment from the microwell chips and washed twice with ice-cold PBS and then lysed for 15 min on ice in 200 µl RIPA buffer (Thermo Fisher Scientific). For disruption of the DNA, the samples were additionally sonicated and then incubated for another 15 min on ice. Protein lysates were centrifuged at 13,000*g* for 5 min at 4 °C and the supernatant was collected. Each 10 µg lysate and 20 µg supernatant were subjected to tryptic digest, applying a modified filter aided sample preparation (FASP) procedure as described[76]. Peptides were collected by centrifugation (10 min at 14,000*g*) and acidified with 0.5% trifluoroacetic acid and stored at −20 °C.

Mass spectrometry measurements. Liquid chromatography–mass spectrometry (LC–MS/MS) analysis was performed in data-dependent acquisition mode. Mass spectrometry data were acquired on a Q-Exactive HF-X mass spectrometer (Thermo Scientific), coupled to a nano-RSLC (Ultimate 3000 RSLC; Dionex). Tryptic peptides were automatically loaded on a C18 trap column (300 µm inner diameter × 5 mm, Acclaim PepMap100 C18, 5 µm, 100 Å, LC Packings) at 30 µl min^{-1} flow rate. For chromatography, a C18 reversed-phase analytical column (nanoEase MZ HSS T3 Column, 100 Å, 1.8 µm, 75 µm × 250 mm; Waters) at 250 nl min^{-1} flow rate in a 95 min non-linear 3–40% acetonitrile gradient in 0.1% formic acid was used. The high-resolution (60,000 full width at half-maximum) mass spectrum was acquired with a mass range from 300 to 1,500 m/z with automatic gain control target set to 3×10^6 and a maximum of 30 ms injection time. From the mass spectrometry pre-scan, the 15 most abundant peptide ions were selected for fragmentation (MS/MS) if at least doubly charged, with a dynamic exclusion of 30 s. MSMS spectra were recorded at 15,000 resolution with automatic gain control target set to 5×10^2 and a maximum of 50 ms injection time. The normalized collision energy was 28, and the spectra were recorded in profile mode.

Protein identification. Proteome Discoverer 2.4 software (Thermo Fisher Scientific; version 2.4.1.15) was used for peptide and protein identification via a database search (Sequest HT search engine) against the Swiss-Prot human database (release 2020_02, 20,349 sequences), considering full tryptic specificity, allowing for one missed tryptic cleavage sites, precursor mass tolerance 10 ppm and fragment mass tolerance 0.02 Da. Carbamidomethylation of Cys was set as a static modification. Dynamic modifications included deamidation of Asn and Gln, oxidation of Met, and a combination of Met loss with acetylation on protein N-terminus. Percolator was used for validating peptide spectrum matches and peptides, accepting only the top-scoring hit for each spectrum, and satisfying the cut-off values for false-discovery rate <1% and posterior error probability <0.01. The final list of proteins complied with the strict parsimony principle.

Label-free quantification. Proteins were quantified on the basis of abundance values for unique peptides. Abundance values were first normalized to the total amount of peptides in each sample to account for sample loading errors. The protein abundances were calculated summing up the abundance values for admissible peptides. In the following only proteins with more than one unique peptide hit were used for downstream analysis.

The secretome data were filtered as follows: first, proteins that were not detected in the parallel recorded proteome or scRNA transcriptome datasets of the duct-like clusters were filtered. Second, proteins that had not been detected previously in the pancreas were filtered out using the 'not detected proteins in the pancreas' protein list of the Human Protein Atlas project[77]. To determine the fraction of proteins that were actively secreted, we matched the PDLO secretome against the refined human secretome[48]. Only proteins with the labels blood secretion and extracellular space were used.

Protein abundance changes within the co-culture experiment were calculated by normalizing the proteomes to the mean abundance levels. The principal components were calculated on the normalized abundances. In the following, the $\log_2$ fold changes of the proteins were calculated between individual culture and co-culture. Proteins that were upregulated in co-culture experiments compared with the respective separately cultured PDLOs or HPaSteCs were further subjected to overrepresentation analyses. Enrichment of upregulated proteins against gene sets in common databases (GO, KEGG and Reactome) was tested using g:Profiler (version: e100_eg47_p14_7733820)[78] browser tool, and EnrichR[79,80] allowed expansion to an EnrichR collective database comprising transcription factor protein–protein interaction networks. The co-culture signalling networks were generated by the X2Kweb[81,82].

Patient material. Archival samples of formalin-fixed paraffin-embedded material and clinical data from clinical reports originate from the previously published ULM cohort, which included 122 patients with resected PDAC[55,56]. Data collection was done retrospectively and included cases from 1997 to 2008. The study was approved by the local ethics committee at Ulm University (reference no. 67, 105/98, 211/2002 and 268/2008).

Blood plasma of patients with metastasizing PDAC was provided by the biobank of Ulm University Hospital. A group of healthy subjects was used as controls. The study was approved by the local ethics committee at Ulm University (reference no. 159/19). Written informed consent of all patients was given for material extraction and scientific use.

Enzyme-linked immunosorbent assay. Levels of human FLNB in PDAC patient serum were analysed using the FLNB ELISA kit (MyBioSource, MBS731914) according to the manufacturer's guidelines. Before the assay, plasma was centrifuged at 1,000*g* for 15 min at 4 °C and the undiluted supernatant was added in duplicates to the ELISA plate. Absorbance at 450 nm was measured with Tecan Infinite M200 Pro plate reader. Concentration of the samples was interpolated from the standard curve that was determined within the same experiment run. The results and patient characteristics are shown in Supplementary Data 5. Statistical significance between the control patients and PDAC patients with grade 2 and 3 tumours was calculated by *t*-test (Fig. 8h). One patient with a tumour grading of 2–3 was excluded for the calculation of statistical significance.

Image analysis. Immunofluorescence, immunohistochemistry and bright-field images were cropped, rotated, aligned, and enlarged (with black background to unify the picture size), and brightness and contrast was edited with ImageJ. The measurements of the organoid diameters for the comparison of different cell numbers and well diameters were performed in ImageJ. In Fig. 1e, at least 58 3D pancreatic-progenitor aggregates from three different microwell chip arrays were measured for each condition. In Supplementary Fig. 2b, 3D hiPSC aggregates from four technical replicates were measured over 3 d. Size changes were analysed by one-sided Student's *t*-test in R. Normal distribution was confirmed by the Shapiro–Wilk test. For the image analysis and editing, ImageJ version 1.52p was used[83].

Sample preparation for scRNA-seq. While pancreatic progenitors at day 13 were collected with TrypLE Select as described above, organoids on the microwell chip were collected on days 14, 16, 20, 23, 27 (samples from experiment 2: 600 cells, 300 µm microwell diameter) and 31 (samples from experiment 1: 300 cells, 300 µm

microwell diameter and 600 cells, 600 µm microwell diameter) by washing the microwell chip three times with PBS. For the dissociation of PDLOs into single cells, organoids were incubated in Accutase for 30–45 min at 37 °C. In experiment 2, single cells were cryo-preserved in DMEM with 10% heat-inactivated FBS (Thermo Fisher Scientific) and 10% DMSO based on a previously described scRNA-seq sample preparation protocol[84]. For sequencing, cryo-preserved cells were thawed in DMEM:F12 and then live–dead filtered as described in the 10x Genomics protocol CG000093. Cells from Experiment 1 (Fig. 2a) were not cryo-preserved or filtered, but directly processed for actual scRNA-seq measurements. An RNA library was generated using Chromium Single Cell 3′ library and Gel Bead Kit v3.1 (10x Genomics). The amplified cDNA library was sequenced on a NovaSeq 6000 S2 flow cell from Illumina. The sequenced cell numbers are presented in Supplementary Fig. 6b.

scRNA-seq data pre-processing. Raw sequencing data files were demultiplexed, aligned (reference genome hg38_ensrel96), filtered, barcodes and UMIs were counted, and subjected to a quality filter with CellRanger (10x Genomics). The pre-processing and downstream analysis were performed with the package Scanpy API[85] in Python with default parameters, unless stated otherwise. First, dead or stressed cells, identified by a percentage of mitochondrial genes higher than 15%, were filtered out. Next, cells with less than 1,200 or more than 10^4 expressed genes and genes expressed in less than 3 cells were excluded. Then, the datasets from different days and experiments were concatenated, normalized to 10^4 gene counts per cell and log-transformed. Batch effects were corrected using ComBat. Later, the top 4,000 highly variable genes were used for the downstream analysis. As discussed by Luecken and Theis[86], we corrected for the total gene counts, percentage of mitochondrial genes, and the cell cycle distribution of S, G2 and M phase to investigate differentiation-dependent changes on the transcriptome level.

Dimensionality reduction, clustering, and cell-type annotation. The single-cell neighbourhood graph was computed with the first 50 principal components and 10 nearest neighbours and the cells were clustered with the Louvain algorithm[87] at a resolution of 0.4. For visualization, the dimensionality of the data was reduced using UMAP[88]. For cell-type annotation, 300 DEGs for each of the nine Louvain clusters were calculated by ranking the clusters against all remaining cells with the *t*-test method (Supplementary Data 1). The clusters were then annotated on the basis of known marker genes.

RNA velocity through dynamical modelling. To investigate developmental trajectories, we analysed the RNA velocity by recovering directed dynamic gene information through splicing kinetics. Information such as clustering and UMAP coordinates were retrieved from the Scanpy analysis. The pre-processing and downstream analysis were performed with scVelo[40] using default parameters. Splice variants and cells were filtered, normalized, and logarithmized with the function scv.pp.filter_and_normalize (parameters: min_cells=3, min_counts=200, min_shared_counts=20, n_top_genes=500). In a subsequent step, the moments, based on the connectivities, were calculated with 30 principal component analyses and 30 neighbours. After recovering the dynamics, the latent time was calculated with a root cell from day 13. On the basis of this latent time, the velocity was calculated as a dynamical model[40].

For the poly fit from Fig. 5e, we excluded the endocrine and the endothelial cell clusters, as well as all cells from the progenitor clusters with a latent time higher than 0.5. This mainly excluded the progenitor cells present at late time points. Afterwards, the cells were sorted by their latent time and the gene expression was fitted to a third-degree polynomial following the code published by Bastidas-Ponce et al.[89].

Enriched gene expression of gene sets. The gene-enrichment UMAP plots from Fig. 8c and Supplementary Fig. 9 were generated using the scanpy command sc.tl.score_genes. The score function subtracts the average expression of a set of genes with a reference gene-set expression, randomly sampled from the whole gene pool. The gene lists for the pathway analysis were downloaded with the R package KEGGREST[90].

Integration of primary pancreas datasets. For the integration of the primary pancreas, three human datasets were used. While GSE84133[24] (human samples GSM2230757, GSM2230759 and GSM2230760) and GSE81547[23] focused mainly on endocrine cells, GSE131886[26] described more ductal cell types. Before the datasets were concatenated, they were preprocessed, clustered and aligned as described for the PDLO scRNA-seq data. To calculate the neighbourhood graph, 32 principal component analyses (based on an elbow plot) and 20 nearest neighbours were considered. For integration and correction of the datasets, we applied bbknn to the datasets (neighbors_within_batch=5, n_pcs=32, trim=0, copy=True) and then re-clustered the cells with the Louvain algorithm[87] at a resolution of 1.3.

Re-clustering of the GSE131886 dataset. To further investigate our identified duct-like cell-cluster markers, the GSE131886[26] dataset was re-clustered in a similar way to our main analysis. Cells with fewer than 800 different genes and more than 15% mitochondrial genes counts were filtered out. For the re-clustering a Louvain algorithm with a resolution of 0.06 was applied, and 2,000 variable genes and 27 principal components were taken into account.

Software specifications. The scRNA-seq alignment was run in CellRanger version 3.0.1 and the analyses were run in Python 3.7.4 with Scanpy API version 1.4.4 or 1.5.1, anndata version 0.6.22 or 0.7.4, umap version 0.3.10, numpy version 1.17.4, scipy version 1.5.1, pandas version 0.25.3 or 1.0.5, scikit-learn version 0.22, statsmodels version 0.10.1, Python-igraph version 0.7.1, Louvain version 0.6.1, scvelo version 0.1.26 development, matplotlib version 3.2.1, seaborn version 0.9.0, loompy version 3.0.6, XlsxWriter version 1.2.6, bbknn version 1.3.6 and scrublet version 0.2.1.

The plots in Figs. 1 and 8 and Supplementary Fig. 2 and 12 were generated in RStudio with R version 3.6.0 with the R packages readxl version 1.3.1, ggplot2 version 3.3.0, dplyr version 1.0.4, survminer version 0.4.8, ggpubr version 0.4.0, reshape2 version 1.4.4, survival version 3.1-12 and ggsignif version 0.6.0. Dot plots in Fig. 8e and bar graphs in Supplementary Fig. 12b were generated using GraphPad Prism version 8.4.3. Principal component plots (Supplementary Fig. 11b) were calculated with stats version 3.6.0 and plotted with factoextra version 1.0.7.

Reporting Summary. Further information on research design is available in the Nature Research Reporting Summary linked to this article.

Data availability

The main data supporting the results in this study are available within the paper and its Supplementary Information. Raw data, read counts and the analysed datasets from scRNA-seq can be accessed from the Gene Expression Omnibus repository using the accession code GSE162547. Mass spectrometry data have been deposited on the PRIDE database and can be accessed with the identifier PXD024461.

Code availability

The code for scRNA-seq analysis is available on Zenodo at https://doi.org/10.5281/zenodo.4738625.

Received: 27 August 2020; Accepted: 1 June 2021;
Published online: 08 July 2021

References

1. Lee, M. G., Ohana, E., Park, H. W., Yang, D. & Muallem, S. Molecular mechanism of pancreatic and salivary gland fluid and HCO_3 secretion. *Physiol. Rev.* **92**, 39–74 (2012).
2. Hohwieler, M. et al. Stem cell-derived organoids to model gastrointestinal facets of cystic fibrosis. *United European Gastroenterol. J.* **5**, 609–624 (2017).
3. Ferreira, R. M. M. et al. Duct- and acinar-derived pancreatic ductal adenocarcinomas show distinct tumor progression and marker expression. *Cell Rep.* **21**, 966–978 (2017).
4. Bailey, J. M. et al. p53 mutations cooperate with oncogenic Kras to promote adenocarcinoma from pancreatic ductal cells. *Oncogene* **35**, 4282–4288 (2016).
5. Lee, A. Y. L. et al. Cell of origin affects tumour development and phenotype in pancreatic ductal adenocarcinoma. *Gut* **68**, 487–498 (2019).
6. Siegel, R. L., Miller, K. D. & Jemal, A. Cancer statistics, 2019. *CA Cancer J. Clin.* **69**, 7–34 (2019).
7. Boj, S. F. et al. Organoid models of human and mouse ductal pancreatic cancer. *Cell* **160**, 324–338 (2015).
8. Huch, M. et al. Unlimited in vitro expansion of adult bi-potent pancreas progenitors through the Lgr5/R-spondin axis. *EMBO J.* **32**, 2708–2721 (2013).
9. Tuveson, D. & Clevers, H. Cancer modeling meets human organoid technology. *Science* **364**, 952–955 (2019).
10. Frappart, P. O. et al. Pancreatic cancer-derived organoids—a disease modeling tool to predict drug response. *United European Gastroenterol J.* **8**, 594–606 (2020).
11. Tiriac, H. et al. Organoid profiling identifies common responders to chemotherapy in pancreatic cancer. *Cancer Disco.* **8**, 1112–1129 (2018).
12. Georgakopoulos, N. et al. Long-term expansion, genomic stability and in vivo safety of adult human pancreas organoids. *BMC Dev. Biol.* **20**, 4 (2020).
13. Boj, S. F. et al. Model organoids provide new research opportunities for ductal pancreatic cancer. *Mol. Cell. Oncol.* **3**, e1014757 (2016).
14. Hohwieler, M. et al. Human pluripotent stem cell-derived acinar/ductal organoids generate human pancreas upon orthotopic transplantation and allow disease modelling. *Gut* **66**, 473–486 (2017).
15. Huang, L. et al. Ductal pancreatic cancer modeling and drug screening using human pluripotent stem cell- and patient-derived tumor organoids. *Nat. Med.* **21**, 1364–1371 (2015).
16. Zhou, Q. et al. A multipotent progenitor domain guides pancreatic organogenesis. *Dev. Cell* **13**, 103–114 (2007).

17. Villani, V. et al. SOX9+/PTF1A+ cells define the tip progenitor cells of the human fetal pancreas of the second trimester. *Stem Cells Transl. Med.* **8**, 1249–1264 (2019).
18. Schaffer, A. E., Freude, K. K., Nelson, S. B. & Sander, M. Nkx6 transcription factors and Ptf1a function as antagonistic lineage determinants in multipotent pancreatic progenitors. *Dev. Cell* **18**, 1022–1029 (2010).
19. Jennings, R. E. et al. Development of the human pancreas from foregut to endocrine commitment. *Diabetes* **62**, 3514–3522 (2013).
20. Breunig, M. et al. Modelling plasticity and dysplasia of pancreatic ductal organoids derived from human pluripotent stem cells. *Cell Stem Cell* **28**, 1105–1124 (2021).
21. Huang, L. et al. Commitment and oncogene-induced plasticity of human stem cell-derived pancreatic acinar and ductal organoids. *Cell Stem Cell* **28**, 1090–1104 (2021).
22. The Tabula Muris Consortium Single-cell transcriptomics of 20 mouse organs creates a Tabula Muris. *Nature* **562**, 367–372 (2018).
23. Enge, M. et al. Single-cell analysis of human pancreas reveals transcriptional signatures of aging and somatic mutation patterns. *Cell* **171**, 321–330 (2017).
24. Baron, M. et al. A single-cell transcriptomic map of the human and mouse pancreas reveals inter- and intra-cell population structure. *Cell Syst.* **3**, 346–360 (2016).
25. Muraro, M. J. et al. A single-cell transcriptome atlas of the human pancreas. *Cell Syst.* **3**, 385–394 (2016).
26. Qadir, M. M. F. et al. Single-cell resolution analysis of the human pancreatic ductal progenitor cell niche. *Proc. Natl Acad. Sci. USA* **117**, 10876–10887 (2020).
27. Segerstolpe, Å. et al. Single-cell transcriptome profiling of human pancreatic islets in health and type 2 diabetes. *Cell Metab.* **24**, 593–607 (2016).
28. Wang, Y. J. et al. Single-cell transcriptomics of the human endocrine pancreas. *Diabetes* **65**, 3028–3038 (2016).
29. Hwang, Y. S. et al. Microwell-mediated control of embryoid body size regulates embryonic stem cell fate via differential expression of WNT5a and WNT11. *Proc. Natl Acad. Sci.* **106**, 16978–16983 (2009).
30. Brandenberg, N. et al. High-throughput automated organoid culture via stem-cell aggregation in microcavity arrays. *Nat. Biomed. Eng.* **4**, 864–874 (2020).
31. Freyer, J. P. Role of necrosis in regulating the growth saturation of multicellular spheroids. *Cancer Res.* **48**, 2432–2439 (1988).
32. Crisera, C. A. et al. Expression and role of laminin-1 in mouse pancreatic organogenesis. *Diabetes* **49**, 936–944 (2000).
33. Miner, J. H. & Yurchenco, P. D. Laminin functions in tissue morphogenesis. *Annu. Rev. Cell Dev. Biol.* **20**, 255–284 (2004).
34. Jiang, F. X., Cram, D. S., DeAizpurua, H. J. & Harrison, L. C. Laminin-1 promotes differentiation of fetal mouse pancreatic beta-cells. *Diabetes* **48**, 722–730 (1999).
35. Kopp, J. L. et al. Progenitor cell domains in the developing and adult pancreas. *Cell Cycle* **10**, 1921–1927 (2011).
36. Kopp, J. L. et al. Sox9$^+$ ductal cells are multipotent progenitors throughout development but do not produce new endocrine cells in the normal or injured adult pancreas. *Development* **138**, 653–665 (2011).
37. Pan, F. C. & Wright, C. Pancreas organogenesis: from bud to plexus to gland. *Dev. Dyn.* **240**, 530–565 (2011).
38. Nair, G. & Hebrok, M. Islet formation in mice and men: lessons for the generation of functional insulin-producing β-cells from human pluripotent stem cells. *Curr. Opin. Genet. Dev.* **32**, 171–180 (2015).
39. Inada, A., Nienaber, C., Fonseca, S. & Bonner-Weir, S. Timing and expression pattern of carbonic anhydrase II in pancreas. *Dev. Dyn.* **235**, 1571–1577 (2006).
40. Bergen, V., Lange, M., Peidli, S., Wolf, F. A. & Theis, F. J. Generalizing RNA velocity to transient cell states through dynamical modeling. *Nat. Biotechnol.* **38**, 1408–1414 (2020).
41. La Manno, G. et al. RNA velocity of single cells. *Nature* **560**, 494–498 (2018).
42. Puri, S., Folias, A. E. & Hebrok, M. Plasticity and dedifferentiation within the pancreas: development, homeostasis, and disease. *Cell Stem Cell* **16**, 18–31 (2015).
43. George, N. M., Day, C. E., Boerner, B. P., Johnson, R. L. & Sarvetnick, N. E. Hippo signaling regulates pancreas development through inactivation of Yap. *Mol. Cell. Biol.* **32**, 5116–5128 (2012).
44. Qu, H. et al. Laminin 411 acts as a potent inducer of umbilical cord mesenchymal stem cell differentiation into insulin-producing cells. *J. Transl. Med.* **12**, 135 (2014).
45. Mamidi, A. et al. Mechanosignalling via integrins directs fate decisions of pancreatic progenitors. *Nature* **564**, 114–118 (2018).
46. Cirulli, V. et al. Expression and function of $\alpha_v\beta_3$ and $\alpha_v\beta_5$ integrins in the developing pancreas: roles in the adhesion and migration of putative endocrine progenitor cells. *J. Cell Biol.* **150**, 1445–1460 (2000).
47. Erkan, M. et al. StellaTUM: current consensus and discussion on pancreatic stellate cell research. *Gut* **61**, 172–178 (2012).
48. Uhlén, M. et al. The human secretome. *Sci. Signal* **12**, eaaz0274 (2019).
49. Uhlen, M. et al. A pathology atlas of the human cancer transcriptome. *Science* **357**, eaan2507 (2017).
50. Zubair, H. et al. Proteomic analysis of MYB-regulated secretome identifies functional pathways and biomarkers: potential pathobiological and clinical implications. *J. Proteome Res.* **19**, 794–804 (2020).
51. Bandaru, S. et al. Targeting filamin B induces tumor growth and metastasis via enhanced activity of matrix metalloproteinase-9 and secretion of VEGF-A. *Oncogenesis* **3**, e119 (2014).
52. Iguchi, Y. et al. Filamin B enhances the invasiveness of cancer cells into 3D collagen matrices. *Cell Struct. Funct.* **40**, 61–67 (2015).
53. Surcel, A. et al. Targeting mechanoresponsive proteins in pancreatic cancer: 4-hydroxyacetophenone blocks dissemination and invasion by activating MYH14. *Cancer Res.* **79**, 4665–4678 (2019).
54. Arnold, F. et al. RINT1 regulates SUMOylation and the DNA damage response to preserve cellular homeostasis in pancreatic cancer. *Cancer Res.* **81**, 1758–1774 (2021).
55. Feld, F. M. et al. GOT1/AST1 expression status as a prognostic biomarker in pancreatic ductal adenocarcinoma. *Oncotarget* **6**, 4516–4526 (2015).
56. Schmid, S. J. et al. Absence of FLICE-inhibitory protein is a novel independent prognostic marker for very short survival in pancreatic ductal adenocarcinoma. *Pancreas* **42**, 1114–1119 (2013).
57. Hirsch, F. R. et al. Epidermal growth factor receptor in non-small-cell lung carcinomas: correlation between gene copy number and protein expression and impact on prognosis. *J. Clin. Oncol.* **21**, 3798–3807 (2003).
58. Kleger, A., Perkhofer, L. & Seufferlein, T. Smarter drugs emerging in pancreatic cancer therapy. *Ann. Oncol.* **25**, 1260–1270 (2014).
59. Reichert, M., Blume, K., Kleger, A., Hartmann, D. & von Figura, G. Developmental pathways direct pancreatic cancer initiation from its cellular origin. *Stem Cells Int.* **2016**, 9298535 (2016).
60. Hassid, B. G. et al. Absence of pancreatic intraepithelial neoplasia predicts poor survival after resection of pancreatic cancer. *Pancreas* **43**, 1073–1077 (2014).
61. Bremer, S. C. B. et al. Enhancer of zeste homolog 2 in colorectal cancer development and progression. *Digestion* **102**, 227–235 (2021).
62. Li, J. et al. An alternative splicing switch in FLNB promotes the mesenchymal cell state in human breast cancer. *eLife* **7**, e37184 (2018).
63. Driehuis, E. et al. Pancreatic cancer organoids recapitulate disease and allow personalized drug screening. *Proc. Natl Acad. Sci. USA* **116**, 26580–26590 (2019).
64. Co, J. Y. et al. Controlling epithelial polarity: a human enteroid model for host–pathogen interactions. *Cell Rep.* **26**, 2509–2520.e2504 (2019).
65. Veres, A. et al. Charting cellular identity during human in vitro β-cell differentiation. *Nature* **569**, 368–373 (2019).
66. Krentz, N. A. J. et al. Single-cell transcriptome profiling of mouse and hESC-derived pancreatic progenitors. *Stem Cell Rep.* **11**, 1551–1564 (2018).
67. Petersen, M. B. K. et al. Single-cell gene expression analysis of a human ESC model of pancreatic endocrine development reveals different paths to β-cell differentiation. *Stem Cell Rep.* **9**, 1246–1261 (2017).
68. Wang, J., Yuan, R., Zhu, X. & Ao, P. Adaptive landscape shaped by core endogenous network coordinates complex early progenitor fate commitments in embryonic pancreas. *Sci. Rep.* **10**, 1112 (2020).
69. Chen, C. et al. Evidence of a developmental origin for β-cell heterogeneity using a dual lineage-tracing technology. *Development* **146**, dev164913 (2019).
70. Larsen, H. L. et al. Stochastic priming and spatial cues orchestrate heterogeneous clonal contribution to mouse pancreas organogenesis. *Nat. Commun.* **8**, 605 (2017).
71. Gitlin, L., Schulze, P. & Belder, D. Rapid replication of master structures by double casting with PDMS. *Lab Chip* **9**, 3000–3002 (2009).
72. Nostro, M. C. et al. Efficient generation of NKX6-1$^+$ pancreatic progenitors from multiple human pluripotent stem cell lines. *Stem Cell Rep.* **4**, 591–604 (2015).
73. Mohammad Rezazadeh, F. et al. Fast free of acrylamide clearing tissue (FACT) for clearing, immunolabelling and three-dimensional imaging of partridge tissues. *Microsc. Res. Tech.* **81**, 1374–1382 (2018).
74. John, T., Liu, G. & Tsao, M. S. Overview of molecular testing in non-small-cell lung cancer: mutational analysis, gene copy number, protein expression and other biomarkers of EGFR for the prediction of response to tyrosine kinase inhibitors. *Oncogene* **28**, S14–S23 (2009).
75. Jesnowski, R. et al. Immortalization of pancreatic stellate cells as an in vitro model of pancreatic fibrosis: deactivation is induced by matrigel and *N*-acetylcysteine. *Lab Invest.* **85**, 1276–1291 (2005).
76. Livnat-Levanon, N. et al. Reversible 26S proteasome disassembly upon mitochondrial stress. *Cell Rep.* **7**, 1371–1380 (2014).
77. Uhlén, M. et al. Tissue-based map of the human proteome. *Science* **347**, 1260419 (2015).
78. Raudvere, U. et al. g:Profiler: a web server for functional enrichment analysis and conversions of gene lists (2019 update). *Nucleic Acids Res.* **47**, W191–w198 (2019).

79. Chen, E. Y. et al. Enrichr: interactive and collaborative HTML5 gene list enrichment analysis tool. *BMC Bioinf.* **14**, 128 (2013).
80. Kuleshov, M. V. et al. Enrichr: a comprehensive gene set enrichment analysis web server 2016 update. *Nucleic Acids Res.* **44**, W90–W97 (2016).
81. Chen, E. Y. et al. Expression2Kinases: mRNA profiling linked to multiple upstream regulatory layers. *Bioinformatics* **28**, 105–111 (2012).
82. Clarke, D. J. B. et al. eXpression2Kinases (X2K) Web: linking expression signatures to upstream cell signaling networks. *Nucleic Acids Res.* **46**, W171–W179 (2018).
83. Schindelin, J. et al. Fiji: an open-source platform for biological-image analysis. *Nat. Methods* **9**, 676–682 (2012).
84. Guillaumet-Adkins, A. et al. Single-cell transcriptome conservation in cryopreserved cells and tissues. *Genome Biol.* **18**, 45 (2017).
85. Wolf, F. A., Angerer, P. & Theis, F. J. SCANPY: large-scale single-cell gene expression data analysis. *Genome Biol.* **19**, 15 (2018).
86. Luecken, M. D. & Theis, F. J. Current best practices in single-cell RNA-seq analysis: a tutorial. *Mol. Syst. Biol.* **15**, e8746 (2019).
87. Blondel, V. D., Guillaume, J.-L., Lambiotte, R. & Lefebvre, E. Fast unfolding of communities in large networks. *J. Stat. Mech: Theory Exp.* **2008**, P10008 (2008).
88. McInnes, L., Healy, J. & Melville, J. UMAP: uniform manifold approximation and projection for dimension reduction. Preprint at https://arxiv.org/abs/1802.03426 (2018).
89. Bastidas-Ponce, A. et al. Comprehensive single cell mRNA profiling reveals a detailed roadmap for pancreatic endocrinogenesis. *Development* **146**, dev173849 (2019).
90. Tenenbaum, D. KEGGREST: client-side REST access to KEGG. R package version 1.24.1 (2019).

Acknowledgements

This work is supported by the Helmholtz Pioneer Campus, the German Ministry of Education and Research (INDIMED-PancChip), the Baden-Württemberg Stiftung (project ExPoChip), ERC (Consolidator Grant Number 772646), Deutsche Forschungsgemeinschaft (DFG) Sachbeihilfe KL 2544/7-1, KL 2544/1-2, KL 2544/5-1, GRK 2254/1 and 2, Heisenberg-Programm KL 2544/6-1, German Cancer Aid (Grant 111879), Else Kröner-Fresenius-Stiftung (supporting A.K. with an Excellence grant and M.H. with a First Application grant) and Bausteinprogramm of Ulm University (granted to M.H.). We thank NK-Optik for instrumental support. We thank M. Löhr (Karolinska Institute) for providing the human pancreatic stellate cells and T. Walzthöni for bioinformatics support provided at the Bioinformatics Core Facility, Institute of Computational Biology, Helmholtz Zentrum München.

Author contributions

S.W., M.B., M.H., A.K. and M. Meier designed the study. S.W. designed and produced the microwell chips, based on work from M. Moussus. S.W., M.B., J.M. and M.H. executed the biological experiments. S.W., M.B., M.H. and T.G. did the imaging and image analysis. S.W., M.S. and H.L. performed the scRNA-seq processing and S.W. did the analysis. C.v.T. and S.M.H. did the mass spectrometric measurements and data processing. S.E.W. and P.M. stained and evaluated the FLNB patient cohort. L.S. and T.S. took the serum samples of the PDAC patient cohort and M.H. performed the ELISA. S.W., M.B. and M. Meier analysed the MS/MS and FLNB screening results. M.H., A.K. and M. Meier received the funding and supervised the study. The manuscript was written by S.W., M.B., M.H., A.K. and M. Meier. All authors corrected and approved the paper.

Competing interests

The authors declare no competing interests.

Additional information

Supplementary information The online version contains supplementary material available at https://doi.org/10.1038/s41551-021-00757-2.

Correspondence and requests for materials should be addressed to M.H., A.K. or M.M.

Peer review information *Nature Biomedical Engineering* thanks the anonymous reviewers for their contribution to the peer review of this work. Peer reviewer reports are available.

Reprints and permissions information is available at www.nature.com/reprints.

Publisher's note Springer Nature remains neutral with regard to jurisdictional claims in published maps and institutional affiliations.

nature research

Corresponding author(s): Matthias Meier, Alexander Kleger and Meike Hohwieler

Last updated by author(s): May 27, 2021

Reporting Summary

Nature Research wishes to improve the reproducibility of the work that we publish. This form provides structure for consistency and transparency in reporting. For further information on Nature Research policies, see our Editorial Policies and the Editorial Policy Checklist.

Statistics

For all statistical analyses, confirm that the following items are present in the figure legend, table legend, main text, or Methods section.

n/a	Confirmed	
☐	☒	The exact sample size (*n*) for each experimental group/condition, given as a discrete number and unit of measurement
☐	☒	A statement on whether measurements were taken from distinct samples or whether the same sample was measured repeatedly
☐	☒	The statistical test(s) used AND whether they are one- or two-sided *Only common tests should be described solely by name; describe more complex techniques in the Methods section.*
☒	☐	A description of all covariates tested
☐	☒	A description of any assumptions or corrections, such as tests of normality and adjustment for multiple comparisons
☐	☒	A full description of the statistical parameters including central tendency (e.g. means) or other basic estimates (e.g. regression coefficient) AND variation (e.g. standard deviation) or associated estimates of uncertainty (e.g. confidence intervals)
☐	☒	For null hypothesis testing, the test statistic (e.g. *F*, *t*, *r*) with confidence intervals, effect sizes, degrees of freedom and *P* value noted *Give P values as exact values whenever suitable.*
☒	☐	For Bayesian analysis, information on the choice of priors and Markov chain Monte Carlo settings
☒	☐	For hierarchical and complex designs, identification of the appropriate level for tests and full reporting of outcomes
☒	☐	Estimates of effect sizes (e.g. Cohen's *d*, Pearson's *r*), indicating how they were calculated

Our web collection on statistics for biologists contains articles on many of the points above.

Software and code

Policy information about availability of computer code

Data collection	All microscope images were obtained with the Zeiss Axio Observer LSM 880 or Z1 with either Zen 2.3 SP1 FP1 (black) or Zen 2 (blue). IHC images were captured with a Leica Typ DM5500, digital camera DFC 420C with the LAS software Leica application Suite Version 3.1.0. Chip pictures were taken with a Nikon D7200. Proteome Discoverer 2.4 software (Thermo Fisher Scientific; version 2.4.1.15) was used for peptide and protein identification via a database search (Sequest HT search engine) against the Swissprot human database (Release 2020_02, 20432 sequences).
Data analysis	The scRNA-seq alignment was run in CellRanger version 3.0.1 and the analyses were run in python 3.7.4 with Scanpy API version 1.4.4 or 1.5.1, anndata version 0.6.22 or 0.7.4, umap version 0.3.10, numpy version 1.17.4, scipy version 1.5.1, pandas version 0.25.3 or 1.0.5, scikit-learn version 0.22, statsmodels version 0.10.1, python-igraph version 0.7.1, louvain version 0.6.1, scvelo version 0.1.26 development, matplotlib version 3.2.1, seaborn version 0.9.0, loompy version 3.0.6, XlsxWriter version 1.2.6, bbknn version 1.3.6 and scrublet version 0.2.1. The plots from Fig. 1 and Supplementary Fig. 2 were generated in RStudio with R version 3.6.0 with the R packages readxl version 1.3.1, ggplot2 version 3.3.0 and ggsignif version 0.6.0. The codes used for the scRNA-seq analysis are available on Zenodo at https://doi.org/10.5281/zenodo.4738625 ELISA results were analysed using GraphPad Prism 8 (GraphPad Software, San Diego, California USA, www.graphpad.com). For the image analysis and editing, ImageJ version 1.52p and ZEN Blue imaging software (ZEISS) was used.

For manuscripts utilizing custom algorithms or software that are central to the research but not yet described in published literature, software must be made available to editors and reviewers. We strongly encourage code deposition in a community repository (e.g. GitHub). See the Nature Research guidelines for submitting code & software for further information.

Data

Policy information about availability of data

All manuscripts must include a data availability statement. This statement should provide the following information, where applicable:

- Accession codes, unique identifiers, or web links for publicly available datasets
- A list of figures that have associated raw data
- A description of any restrictions on data availability

The main data supporting the results in this study are available within the paper and its Supplementary Information. Raw data, read counts and the analysed datasets from scRNA-seq can be accessed from the Gene Expression Omnibus (https://www.ncbi.nlm.nih.gov/geo/query/acc.cgi?acc=GSE162547) repository via the accession code GSE162547. Mass-spectrometry data have been deposited on the PRIDE database (https://www.ebi.ac.uk/pride/archive/projects/PXD024461) and can be accessed via the identifier PXD024461.

Field-specific reporting

Please select the one below that is the best fit for your research. If you are not sure, read the appropriate sections before making your selection.

☒ Life sciences ☐ Behavioural & social sciences ☐ Ecological, evolutionary & environmental sciences

For a reference copy of the document with all sections, see nature.com/documents/nr-reporting-summary-flat.pdf

Life sciences study design

All studies must disclose on these points even when the disclosure is negative.

Sample size	No statistical methods were used to calculate sample sizes for our biological experiments. In the scRNA-seq experiments, the number of analysed cells was selected according to standard protocols, on the basis of relevant previous studies, and to comply with technical requirements. Difficulties in the retrieval of cells, sample preparation, or in the quality filter applied during data processing resulted in a variable number of sequenced cells, ranging from 500 to 6,700 cells (Supplementary Fig. 6a). The number of PDAC patients analysed in Fig. 8e–g and in Supplementary Fig. 12c was specified by the previously published ULM cohort. Sample size for the analysis of FLNB serum levels (Fig. 8h) was limited by availability of (material from) donors/PDAC patients. Precise numbers and details on the experimental replicates are provided in the paper.
Data exclusions	Some cells from scRNA-seq were filtered out as part of a standard quality-check procedure. For the analysis of the PDAC patient cohort, twelve patients were excluded because of the absence of tumour in FFPE tumour specimens (Fig. 8f,g). In Fig. 8h, one patient with a tumor grading of 2–3 could not be assigned to one of the predetermined groups (grading ≤2 or ≥3) and was therefore excluded for the calculation of statistical significance.
Replication	In general, the results of biological experiments were determined from 2 or more technical or biological replicates, with numbers stated in Methods and in the figure captions. The findings of scRNA-seq analysis could be reproduced in a second independent ductal differentiation experiment (Fig. 4d). Regarding the reproduction of the expensive and comprehensive analyses over the time series of differentiation, only the end stages were assessed. To identify duct-like cell subtypes in healthy human primary pancreas tissue and in tissue from pancreatitis patients (Fig. 5c,d, and Suppl. Fig. 7b,c), samples of at least two different donors were analysed for each condition.
Randomization	Randomization was not relevant to the study.
Blinding	The data analyses were not blinded because the analyses were based on quantitative measurements.

Reporting for specific materials, systems and methods

We require information from authors about some types of materials, experimental systems and methods used in many studies. Here, indicate whether each material, system or method listed is relevant to your study. If you are not sure if a list item applies to your research, read the appropriate section before selecting a response.

Materials & experimental systems

n/a	Involved in the study
☐	☒ Antibodies
☐	☒ Eukaryotic cell lines
☒	☐ Palaeontology and archaeology
☐	☒ Animals and other organisms
☐	☒ Human research participants
☒	☐ Clinical data
☒	☐ Dual use research of concern

Methods

n/a	Involved in the study
☒	☐ ChIP-seq
☐	☒ Flow cytometry
☒	☐ MRI-based neuroimaging

Antibodies

Antibodies used

Primary antibodies:
acTUB (host: rabbit, dilution: 1:1000, Abcam, ab179484, clone: EPR16772, lot: GR3240369-6), AMY2A (host: rabbit, dilution: 1:1000, Sigma, A8273-1VL, polyclonal, lot: 068K4796), AQP5 (host: rabbit, dilution: 1:200, Abcam, ab92320, clone: EPR3747, lot: GR3273694-1), ARL13B (host: mouse, dilution: 1:1000, Abcam, ab136648, clone: N295B/66, lot: GR3272548-1), BICC1 (host: rabbit, dilution: 1:75, Sigma, NBP194171, polyclonal), c-KIT (host: mouse, dilution: 1:100, Invitrogen, CD11705, clone: 104D2, lot: 2086609), CA2 (host: rabbit, dilution: 1:500, Abcam, ab124687, clone: EPR5195, lot: GR155503-7), CDH1 (host: mouse, dilution: 1:1000, BD Bioscience, 610182, clone: 36, lot: 9315423), CDH1 (host: rabbit, dilution: 1:200, Cell Signaling, 3195, clone: 24E10, lot: 13), CFTR (host: mouse, dilution: 1:200, R&D, MAB1660, clone: 13-1, lot: BLG022005A), CFTR (host: rabbit, dilution: 1:200-800, Cell Signaling, 78335, clone: D6W6L, lot: 1), CHGA (host: mouse, dilution: 1:200, Dako, M0869, clone: DAK-A3, lot: 20081824), CLDN1 (host: rabbit, dilution: 1:100, Abcam, ab15098, polyclonal, lot: GR282937-1), CLDN1 (host: rat, dilution: 1:200, R&D, MAB4618, clone: 421203, lot: ZZY031912B), COL4A1 (host: rabbit, dilution: 1:500, Abcam, ab6586, polyclonal, lot: GR3350938-1/GR322984-1), CXCR4 (host: mouse, dilution: 1:50, Life Technologies, MHCXCR404, clone: 12G5, lot: 2153692), FLNB (host: rabbit, dilution: 1:50, Merck, HPA004886, polyclonal, lot: 000018297), GATA6 (host: rabbit, dilution: 1:300, Cell Signaling, 5651, clone: D61E4, lot: 5), HNF1B (host: mouse, dilution: 1:100, Abcam, ab236759, clone: CL0374, lot: GR3279363-6), H-Nucleoli (host: mouse, dilution: 1:200, Abcam, ab190710, clone: NM95, lot: GR3269017-3), Ki-67 (host: mouse, dilution: 1:200, Dako, M7240, clone: MIB-1, lot: 20083387), KRT19 (host: mouse, dilution: 1:100, Dako, M08889, clone: RCK108, lot: 20062456/41236534), KRT7 (host: mouse, dilution: 1:200, Dako, M7018, clone: OV-TL, lot: 20064378), KRT8 (host: mouse, dilution: 1:100, BD Bioscience, 345779, clone: CAM5.2, lot: 5292988), MMP1 (host: rabbit, dilution: 150, Abcam, ab52631, clone: EP1247Y, lot: GR3261996-3), MUC1 (host: mouse, dilution: 1:100, Santa Cruz, sc-7313, clone: VU4H5, lot:A2114), MUC1 (host: rabbit, dilution: 1:200, Cell Signaling, 14161, clone: D908K, lot: 1), MUC13 (host: mouse, dilution: 1:500, BioLegend, 363902, clone: TCC16, lot: B190123), MUC2 (host: rabbit, dilution: 1:200, Santa Cruz, sc-7314, clone: Ccp58, lot: 00920), MUC5AC (host: mouse, dilution: 1:100, Santa Cruz, sc-33667, clone: CLH2, lot: J1408), MUC6 (host: mouse, dilution: 1:100, Santa Cruz, sc-33668, clone: CLH5, lot: B0520), NKX6-1 (host: mouse, dilution: 1:150, DSHB Hybridoma, FF55A12 concentrate, clone: FF5A12, lot: AD18110292/AE29446913), NKX6-1-APC (host: mouse, BD Bioscience, dilution: 1:35, clone: R11-560, lot: 1062126), OCT4 (host: mouse, dilution: 1:100, Santa Cruz, sc-5279, clone: C-10, lot: C2014), PDX1 (host: goat, dilution: 1:500, R&D, AF2419, polyclonal, lot: UNY0119031), PDX1 (host: mouse, dilution: 1:35, BD Bioscience, 562161, clone: 658A5, lot: 0058961), SCTR (host: mouse, dilution: 1:100, Atlas Antibodies, HPA007269, polyclonal, lot: A119297/61742), SOX2 (host: mouse, dilution: 1:300, R&D, MAB2018, clone: 245610), SOX9 (host: mouse, dilution: 1:400, Cell Signaling, 82630, clone: D8G8H, lot: 1), SOX9 (host: rabbit, dilution: 1:500, Millipore, AB5535, polyclonal, lot: 3249418/3282152), TFF1 (host: mouse, dilution: 1:100, Novus Biologicals, NBP2-34293, clone: GE2, lot: 7031-1P180627), VIM (host: rabbit, dilution: 1:500, Cell Signaling, 5741, clone: D21H3, lot: 6), ZEB1 (host: mouse, dilution: 1:300, Santa Cruz, sc-515797, clone: H-3, lot: C0520), ZO-1 (host: mouse, dilution: 1:100, Invitrogen, 339100, clone: A12, lot: TL277395), ZO-1 (host: mouse, dilution: 1:200, Invitrogen, 339100-A555, clone: A12, lot: TI277386)

Secondary antibodies:
anti-mouse alexa488 (host: donkey, dilution: 1:2000, Invitrogen, A21202, Lot:2147618), anti-mouse alexa568 (host: donkey, dilution: 1:500, Invitrogen, A10037, Lot:2110843/1820538), anti-rabbit alexa488 (host: donkey, dilution: 1:500, Invitrogen, A21206, Lot:2289872), anti-rabbit atto550 (host: goat, dilution: 1:1000, Sigma Aldrich, 43328, Lot: BCBV1523), anti-rat alexa488 (host: donkey, dilution: 1:800, Invitrogen, A21208, Lot: 2180272), anti-goat alexa488 (host: donkey, dilution: 1:500-800, Invitrogen, A11055, Lot: 2211210)

Validation

Validated on primary human tissue and/or used as recommended by the supplier.

Eukaryotic cell lines

Policy information about cell lines

Cell line source(s)

hiPSCs were established in-house from healthy donor keratinocytes. Written consent of the patient was given for material extraction and scientific use; reprogramming was permitted by the "Ethikkomission" from Ulm University (reference no. 68/11-UBB/bal.)

Human pancreatic stellate cells, isolated from a chronic pancreatitis resection and immortalized by SV40 large T antigen and the catalytic subunit of hTERT (Jesnowski et al., 2005), were kindly provided by Prof. Matthias Löhr (Karolinska Institute).

Authentication

Isolation, culture and pancreatic differentiation of iPSCs, and the study of iPSC derivatives, were approved by the local ethics committee at Ulm University (reference no. 159/19) under the informed consent of donors.

Mycoplasma contamination

Mycoplasma tests were regularly performed on the cell line, with negative results.

Commonly misidentified lines
(See ICLAC register)

No commonly misidentified cell lines were used.

Animals and other organisms

Policy information about studies involving animals; ARRIVE guidelines recommended for reporting animal research

Laboratory animals

All animals were NSG mice (strain: NOD.Cg-Prkdc<scid<tm1Wjl>/SzJ GVO) from Charles River, RRID:BCBC_4142, female, 11-weeks old, with a weight of 25 g.

Wild animals

The study did not involve wild animals.

Field-collected samples

The study did not involve samples collected from the field.

Ethics oversight	All animal work was done under ethical and animal protection regulations of the German animal protection law, and were previously approved by the respective governmental review board of the state of Baden-Württemberg (TVA-1406).

Note that full information on the approval of the study protocol must also be provided in the manuscript.

Human research participants

Policy information about studies involving human research participants

Population characteristics	The previously published ULM cohort included 122 patients with resected pancreatic ductal adenocarcinoma (Schmid et al, Pancreas 2013; Feld et al., Oncotarget 2015). PDACs were classified with the International Union Against Cancer (UICC) according the 7th Edition of the TNM Classification of Malignant Tumors. In few cases, metastatic PDAC has also been resected (Hackert et al., Eur J Surg Oncol 2017). All 110 tumor samples analysed in this study were treatment-naïve. 40 patients received adjuvant chemotherapy after primary resection. In detail: 24 patients received gemcitabine monotherapy and 14 received a combination of gemcitabine with either capecitabine (2 patients), erlotinib (8 patients) or cetuximab (4 patients). 5-Fluorouracil was administered to one patient. One patient received a not-further-specified study drug. FLNB protein expression was determined by immunohistochemistry in 110 samples. Twelve patients were excluded because of the absence of tumour in FFPE tumour specimens. FLNB protein-expression level within the tumour compartment was evaluated by a board-certified pathologist at Ulm University. FLNB expression level was scored from zero (negative) to five (strong). FLNB expression levels were correlated to the clinical characteristics of patients. The analysis of FLNB serum levels was restricted to patients with metastasizing PDAC and healthy control subjects. Detailed patient characteristics are available as Supplementary Information.
Recruitment	Data collection of the ULM cohort (archival samples of FFPE material and clinical data from clinical reports) was done retrospectively, and included cases from 1997 to 2008. Blood plasma from patients was provided by the biobank of Ulm University Hospital.
Ethics oversight	The studies were approved by the local ethics commitee at Ulm University (reference no. 159/19).

Note that full information on the approval of the study protocol must also be provided in the manuscript.

Flow Cytometry

Plots

Confirm that:

☐ The axis labels state the marker and fluorochrome used (e.g. CD4-FITC).

☐ The axis scales are clearly visible. Include numbers along axes only for bottom left plot of group (a 'group' is an analysis of identical markers).

☐ All plots are contour plots with outliers or pseudocolor plots.

☐ A numerical value for number of cells or percentage (with statistics) is provided.

Methodology

Sample preparation	Differentiation efficiencies were controlled on day 3, 9 and 13. The percentage of definitive endoderm cells was assessed by staining the surface marker CXCR4 and c-KIT on day 3. Pancreatic endoderm and pancreas progenitor cells were formaldehyde fixed (4% PFA) (Thermo Fisher Scientific) on day 9 and 13 for intracellular staining of PDX1, and PDX1 + NKX6-1, respectively. Details of the staining procedure have been previously described in Hohwieler et al. (Gut 2017).
Instrument	LSRII flow cytometer (BD Biosciences)
Software	FlowJo (v10; BD Bioscience)
Cell population abundance	Not applicable.
Gating strategy	First, cells were gated on FSC-A/SSC-A; and second, single cells were gated on FSC-H and FSC-A. Positive signal was gated based on isotype controls and undifferentiated hiPSCs as the negative control.

☐ Tick this box to confirm that a figure exemplifying the gating strategy is provided in the Supplementary Information.